Multiscale modeling of thermo-mechanical responses of granular materials: A hierarchical continuum–discrete coupling approach

Shiwei Zhao[a],[*], Jidong Zhao[a], Yuanming Lai[b]

[a] *Department of Civil and Environmental Engineering, Hong Kong University of Science and Technology, Clearwater Bay, Kowloon, Hong Kong*
[b] *State Key Laboratory of Frozen Soil Engineering, Northwest Institute of Eco-Environment and Resources, Chinese Academy of Sciences, Lanzhou, China*

Abstract

A hierarchical multiscale coupling of the finite element method (FEM) and the discrete element method (DEM) is proposed to model coupled thermo-mechanical behavior of granular materials. The DEM is employed to model the thermo-mechanical responses of a representative volume element (RVE, a granular assembly) embedded at a Gauss (quadrature) point of the FEM. The material responses derived from each Gauss point feed two superimposed FEMs to find global solutions subject to two concurrent boundary value problems (BVPs), i.e., heat conduction and mechanical deformation. The two concurrent FEMs exchange information on temperature change and fabric variation at their commonly shared Gauss points. The proposed approach is benchmarked by two examples of transient and steady-state thermal conduction where analytical solutions are available. It is further applied to investigating the thermo-mechanical responses of confined granular columns under cyclic thermal loads with emphasis placed on the effect of boundary condition and inherent anisotropy of a granular column. The proposed approach offers a novel multiscale pathway to model thermo-mechanical responses of granular media based on sound physics.
© 2020 Elsevier B.V. All rights reserved.

Keywords: Multiscale modeling; Granular materials; Thermo-mechanical problem; FEM–DEM coupling

1. Introduction

Granular media are typically complex systems. They consist of discrete particles that form strongly heterogeneous and amorphous internal structures interacting and giving rise to emerging phenomena that distinguish them from solids and fluids. Subjected to external loadings or internal perturbations, granular materials may exhibit sensitive fragility with irrecoverable (plastic) deformation that leads to strong history-dependent behavior [1,2]. For example, sand experiences volumetric contraction and/or dilatancy when subjected to external mechanical loads such as shear, which is well known as dilatancy in soil mechanics [3]. Temperature variation may also cause changes in contacts and fabric among particles, resulting in interesting thermal responses in granular media. Indeed, cyclic thermal

---

* Corresponding author.
  E-mail address: ceswzhao@ust.hk (S. Zhao).

and/or mechanical loadings may induce accumulation of plastic deformation that leads to various distresses such as granular ratcheting, liquefaction, and shakedown [4–7].

The coupling effect of thermal and mechanical behaviors greatly complicates the performance of already complex granular materials, which is relevant to their design, operation, and risk management for critical applications and infrastructures in industry and engineering. One highlighted practice is the application of thermal energy storage (TES) [8] for balancing of energy between day and night or summer and winter as a promising attempt to reduce CO_2 emissions. For example, the packed-bed TES with granular materials such as rocks and sands has been popularly employed in concentrated solar power plants due to its high efficiency and low cost [9]. Another noteworthy application is the so-called energy pile (or thermal pile) that serves as building foundation and meanwhile exchanges thermal energy with its surrounding soils [10]. The granular materials within a TES system, as aforementioned, suffer from cyclic thermo-mechanical loadings. A full understanding of their corresponding responses such as shakedown and stability remains a challenging topic of multidisciplinary research. Indeed, great efforts have been devoted from different disciplines including physics, thermal and geotechnical engineering. Prevailing approaches can be broadly classified into two categories. One is the continuum-based, where a granular material is homogenized as a continuum (with mixture theory employed for further consideration of multi-phase) and is described by various sophisticated constitutive models, most often phenomenological in nature, to characterize its thermo-mechanical response [11,12]. Frequently, these continuum models require the introduction of many model parameters that either lack precise physical meanings or need challenging calibration by experiments in order to capture complicated granular behaviors, such as anisotropy, non-coaxiality, history-dependency, and cyclic hysteresis [13–15]. Nevertheless, continuum-based numerical methods such as the finite element method (FEM), in conjunction with phenomenological constitutive models, have proven to be robust and efficient for large-scale engineering problems. Also, there have been attempts to obtain the constitutive relation with machine learning instead of conventional mathematical models [16]. In contrast to the continuum-based methods, the second category, i.e., the micromechanics-based methods exemplified by the discrete element method (DEM) [17], can capture the discrete nature of granular particles. Indeed, heat transfer through a granular material can be considered as grain-scale heat flows, and the thermally-induced inter-particle force can be captured with a contact force model in DEM [18–20]. In addition, coupling methods such as coupling DEM with the computational fluid dynamics (CFD) [21] have been proposed to consider heat convection through granular materials. However, large-scale (e.g., billions of particles and more) DEM simulations remain computationally too expensive to solve a practical engineering problem, and even worse with additional coupling with CFD [22], although speed-up is possible by parallelization of multi-core CPUs and/or the promising GPU acceleration technique [23].

Marrying the above two approaches to leverage their advantages appears to be appealing, and continuum–discrete coupling has indeed been explored extensively. Among many, the concurrent and hierarchical couplings have been two prevailing schemes. The concurrent coupling scheme typically partitions a domain into a subdomain of interest (e.g., the soils near a pile for a pile installation problem) which is modeled by DEM, while the rest of the domain is modeled by FEM rather than DEM to reduce the computational cost to some extent [24]. Another popular concurrent coupling scheme is the FDEM that has been widely used to simulate the fragmentation of solids subjected to external loadings [25,26], and further extended to model thermally-induced cracking [27] and granular crushing [28]. The second scheme is hierarchical coupling, represented by the hierarchical FEM/DEM [29–32] and the two-scale FEM (FE^2) [33–35], typically using FEM to model an entire macro domain and the DEM or FEM hierarchically embedded to each FEM Gauss point to provide required constitutive responses. Taking the FEM/DEM coupling as an example [14,32,36], the hierarchical coupling approach brings two noteworthy features: (1) the characteristics of a granular material can be readily modeled by FEM with DEM-simulated responses instead of assumed phenomenological constitutive models; and (2) the DEM needs only to solve representative volume elements (RVEs) at a finite number of Gauss points instead of having to deal with the entire domain, thereby considerably reducing the computational cost. Therefore, it is of interest to extend this FEM/DEM coupling approach in consideration of thermal–mechanical effects.

In this study, we propose a hierarchical multiscale approach to modeling the thermo-mechanical responses of granular materials, as a significant extension of our group's previous work [14,32,36,37]. In addition to considering a thermal effect, this new hierarchical multiscale approach has the following two critical new features. One is the model implementations of using non-spherical particles for the RVE due to the significance of particle shape effect [38–41]. The other is the computational challenges in coupling the thermal and mechanical

responses of a granular media in both micro and macro scales. Specifically, at the grain scale, a general thermo-mechanical model will be proposed for non-spherical particles, which enables seamless coupling of the thermal and mechanical effect on an RVE such as thermally-induced stress, deformation, and thermal conductivity change by according deformation. At the macro scale, the thermo-mechanical problem is equivalently split into two concurrent subproblems, i.e., thermal conduction and mechanical response, and are then solved by two concurrent FEMs with the same mesh, respectively. The homogenized thermo-mechanical response of RVEs serves as the constitutive relation of a granular material in conjunction with the two concurrent FEM solvers for smooth micro–macro bridging. Benchmark and demonstrative examples are provided for the proposed hierarchical multiscale approach.

The rest of the paper is organized as follows. Section 2 provides detail of the approach and formulation. The proposed approach is then benchmarked by two examples of transient and steady-state thermal conduction in Section 3. Section 4 further investigates the thermo-mechanical response of a confined granular column, with particular attention placed on the effect of boundary condition and inherent anisotropy. Conclusions are made in Section 5. Tensorial indicial notations and Einstein summation convention are followed in the study, and boldface letters for matrices are used.

2. Approach and formulation

2.1. Governing equations for the macro-scale

2.1.1. Thermal conduction

At the macro scale, a granular material can be regarded as a continuum with anisotropy, in which the heat conduction is expressed by the following differential equation

$$(-k_{ij}T_{,j})_{,i} + \rho c T_{,t} = Q_t \tag{1}$$

where T is the temperature [K]; t is the time [s]; ρc is the bulk volumetric heat capacity [J/(m^3·K)]; k_{ij} is the thermal conductivity tensor [W/(m·K)]; i, j are sequential indices in $\{1, 2, 3\}$ for 3D or $\{1, 2\}$ for 2D; Q_t is a heat source or sink. The heat flux vector q_i is given by a linear combination of the temperature gradients along the x_1, x_2, and x_3 directions [42], i.e.,

$$q_i = -k_{ij}T_{,j} \tag{2}$$

We consider the general boundary and initial conditions for the heat conduction problem as follows

$$T(t) = \bar{T} \quad \text{on} \quad \Gamma_T \tag{3a}$$

$$q(t)_i = \bar{q}_i \quad \text{on} \quad \Gamma_q \tag{3b}$$

$$T(0) = T_{ref} \tag{3c}$$

where Γ_T and Γ_q are the prescribed temperature and heat flux boundaries of the problem domain Ω, respectively; $\bar{T}$ and $\bar{q}_i$ are the prescribed boundary temperature on Γ_T and boundary heat flux on Γ_q, respectively; T_{ref} is the ambient or reference temperature; Eqs. (3a) and (3b) are Dirichlet (fixed temperature) and Neumann (fixed heat flux) boundary conditions, respectively, while Eq. (3c) is the initial condition for temperature distribution at the initial state.

The transient state governed by Eq. (1) with time dependence can be sequentially solved as a series of steady states in a finite difference manner. With the backward Euler scheme, the temperature at time t is expressed as

$$T^{(t)} \approx T^{(t-\Delta t)} + \Delta t T_{,t}^{(t)} \tag{4}$$

where Δt is the differential step of time. Therefore, the governing equation for a steady state during Δt comes out as

$$(-k_{ij}T_{,j}^{(t)})_{,i} + \frac{\rho c}{\Delta t}T^{(t)} = Q_t + \frac{\rho c}{\Delta t}T^{(t-\Delta t)} \tag{5}$$

Multiplying Eq. (5) by a weight function $\omega^{(T)}$ (with zeros on Γ_T) and integrating over the domain Ω with applying integration by parts and Green's formula, the weak form is obtained as follows

$$\int_{\Omega} \omega_{,i}^{(T)} k_{ij} T_{,j}^{(t)} \mathrm{d}\Omega + \int_{\Omega} \omega^{(T)} \frac{\rho c}{\Delta t} T^{(t)} \mathrm{d}\Omega = \int_{\Omega} \omega^{(T)}(Q_t + \frac{\rho c}{\Delta t}T^{(t-\Delta t)})\mathrm{d}\Omega - \int_{\Gamma_q} \omega^{(T)}\bar{q}\mathrm{d}\Gamma \tag{6}$$

In addition, the time step must be sufficiently small to maintain numerical stability and convergence in the coupled thermo-mechanical system. Note that although the backward Euler scheme is unconditionally-stable for the thermal transition, the mechanical system solved by the explicit DEM solver is only conditionally stable. Hence, to avoid possible instability caused to the mechanical system in a thermal transition, the Courant–Friedrichs–Lewy condition is applied as a strong condition for simplicity, and the maximum (critical) time step Δt_m is estimated as

$$\Delta t_m = \frac{l_e^2 \rho c}{bk} \tag{7}$$

where b is an adjustable factor, set to 1 by default; l_e is the minimum element size of a mesh; k is the mean thermal conductivity, i.e., average of the diagonal terms of the thermal conductivity tensor k_{ij}.

2.1.2. Mechanical response

For a macro continuum of granular material, the balance of linear momentum for a quasi-static problem is given as

$$\sigma_{ij,j} + \rho b_i = 0 \tag{8}$$

where σ_{ij} is the Cauchy stress tensor; ρ is the bulk density of materials, and b_i is the body force per unit of mass possibly performed on materials (e.g., gravitational acceleration). The generally encountered boundary conditions are written as

$$u_i = \bar{u}_i \quad \text{on} \quad \Gamma_u \tag{9a}$$

$$\sigma_{ij} n_j = \bar{t}_i \quad \text{on} \quad \Gamma_t \tag{9b}$$

where n_j is the boundary outward normal of the domain Ω; $\bar{u}_i$ and $\bar{t}_i$ are the prescribed material displacement on Γ_u and boundary traction on Γ_t, respectively; Eqs. (9a) and (9b) are Dirichlet and Neumann boundary conditions, respectively.

Multiplying Eq. (8) by a weight function $\omega_i^{(u)}$ (with zeros on Γ_u) and integrating over the domain Ω with applying integration by parts and Green's formula, the weak form is obtained as follows

$$\int_\Omega \omega_{i,j}^{(u)} \sigma_{ij} \mathrm{d}\Omega = \int_\Omega \omega_i^{(u)} \rho b_i \mathrm{d}\Omega + \int_{\Gamma_t} \omega_i^{(u)} \bar{t}_i \mathrm{d}\Gamma \tag{10}$$

2.2. Ingredients at the micro-scale

2.2.1. Thermal conductivity tensor of an assembly

For the convenience of implementation, only the inter-particle heat conduction is considered here, i.e., heat transferring from one grain to another only through their contacts. Empirical and numerical models for thermal conductivity of granular materials have indeed been reported in the literature [18,43–45]; however, most of them focus on establishing an overall thermal conductivity for the entire domain in a specified direction, thereby not suitable for construction of the thermal conductivity tensor. In this work, we introduce an easy-to-use approach for constructing the thermal conductivity tensor for non-spherical particles. Following the basic concept of heat reservoirs for spherical particles used in the commercial code *PFC* [46], the thermal conductivity tensor is deduced as follows. As illustrated in Fig. 1(a), the two contacting particles (exemplified by two ellipses in 2D) and their contact can be regarded as three individual heat reservoirs (note that in *PFC* only two heat reservoirs are introduced). Accordingly, an imaginary heat pipe joining the center of one particle to the contact is introduced. Therefore, the heat flux throughout such a heat pipe is given as

$$q_i = -\frac{\Delta T r_i}{\alpha l^2 A} \tag{11}$$

where l and A are the length and cross-sectional area of the heat pipe, respectively; α is the thermal resistance per length; ΔT is the temperature difference between the two ends of the pipe; r_i is the vector along the heat pipe. Note that the heat flux throughout the contact is along the contact normal within a finite regime (not shown in Fig. 1(a)).

For an entire assembly, a homogeneous heat flux can be obtained with the following volume averaging

$$\langle q_i \rangle = \frac{1}{V} \sum_{p \in V} q_i^{(p)} A^{(p)} l^{(p)} \tag{12}$$

Fig. 1. (a) Heat conduction through an inter-particle contact; (b) thermally-induced contact force due to particle expansion.

where p refers to as the p-th heat pipe, and V is the volume of the assembly. Assuming the mean temperature gradient $\Delta T = r_j T_{,j}$, and substituting Eq. (11) into Eq. (12) with applying the Fourier's law given in Eq. (2), the thermal conductivity tensor is obtained as

$$k_{ij} = \frac{1}{V} \sum_{p=1}^{M} \frac{r_i^{(p)} r_j^{(p)}}{\alpha^{(p)} l^{(p)}} \tag{13}$$

2.2.2. Interaction force between grains

In the DEM implementation, we employ the simple linear spring contact model to establish the relation between contact force and relative displacement for each pair of contacting grains as follows

$$f_i^{\,n} = -k_n u_i^n \tag{14a}$$
$$\Delta f_i^{\,t} = -k_t \delta u_i^t \tag{14b}$$

where $f_i^{\,n}$ and $f_i^{\,t}$ are normal and tangential contact forces along the normal n_i^c and the tangential t_i^c directions at contact c, respectively, referring to Fig. 1(b); $\Delta f_i^{\,t}$ is the incremental tangential contact force at the current time step; k_n and k_t are the normal and tangent contact stiffness, respectively; u_i^n is the penetration depth along contact normal, δu_i^t is the relative tangential displacement of the two contacting particles at the current time step. The contact normal is parallel to the outward normal of the two contacting particles at contact, i.e., the so-called common normal. For non-spherical particles, finding the common normal is an optimization problem, which has been discussed in our previous studies [47,48] and among others [49]. Thus, the detail on the computation of contact geometrical properties such as contact normal, penetration depth and tangential displacement is not presented here for brevity. Moreover, the Coulomb condition of friction is applied to constraining the tangential contact force, i.e.,

$$\sqrt{f_i^{\,t} f_i^{\,t}} \leq \mu \sqrt{f_i^{\,n} f_i^{\,n}} \tag{15}$$

where μ is the coefficient of friction.

With respect to thermally-induced contact force between grains, it remains a challenge to propose a thermal constitutive model as the force–displacement one above. As a workaround, we assume that particles exposed to temperature change will expand or contract in the following manner [7,20,50]:

$$R_i = R_i^{(0)}(1 + \beta \Delta T) \tag{16}$$

where $R_i^{(0)}$ is the initial principal length of a particle at the reference temperature; R_i is the current principal length of a particle at a temperature change ΔT with respect to the reference temperature; β is the linear thermal expansion coefficient. As a consequence, the thermally-induced change in particle profile yields an additional penetration δd_i, referring to Fig. 1(b), thereby resulting in an increase or decrease in contact force (i.e., the thermally-induced contact force) in the presence of the mechanical contact model given in Eq. (14).

2.2.3. Stress and stiffness of an assembly

The averaged (homogenized) macroscopic stress tensor σ_{ij} of a granular assembly is given by the well-established Love equation [51]

$$\sigma_{ij} = \frac{1}{V} \sum_{c \in V} f_i^{\,c} l_j^{\,c} \tag{17}$$

where $f_i^{\,c}$ is the contact force at contact c; $l_j^{\,c}$ is the branch vector joining the two centers of the contacting particles; V is the volume of the entire assembly. With the assumption of uniform deformation, the averaged stiffness tensor can be obtained by partial derivative of the stress tensor with respect to the deformation as [52,53]

$$D_{\alpha\beta\gamma\phi} = \frac{1}{V} \sum_{c \in V} (k_n n_\alpha^c l_\beta^c n_\gamma^c l_\phi^c + k_t t_\alpha^c l_\beta^c t_\gamma^c l_\phi^c) \tag{18}$$

where k_n^c and k_t^c are the normal and tangential contact stiffness at contact c, respectively. The stiffness tensor will serve as the tangent operator in solving the mechanical system in Eq. (20b) with the Newton–Raphson method as in the literature [14,32,36]. Note, of course, that there are some other potential operators having been proposed (see [54]), but not introduced to avoid distractions in the presentation.

2.3. Hierarchical coupling for micro–macro bridging

2.3.1. FEM solvers

For the steady-state thermal conduction, the quasistatic thermo-mechanical problem is split into two concurrent BVPs solved by two FEM solvers on the same mesh. Benefited from the Galerkin FEM, the weight functions ($\omega^{(T)}(\boldsymbol{x})$ and $\boldsymbol{\omega}^{(u)}(\boldsymbol{x})$) and the trial solutions ($T(\boldsymbol{x})$ and $\boldsymbol{u}(\boldsymbol{x})$) can be approximated by the same shape function, i.e.,

$$T(\boldsymbol{x}) \approx \boldsymbol{N}_T \boldsymbol{T}, \quad \omega^{(T)}(\boldsymbol{x}) \approx \boldsymbol{N}_T \boldsymbol{\omega}^{(T)} \tag{19a}$$

$$\boldsymbol{u}(\boldsymbol{x}) \approx \boldsymbol{N}_u \boldsymbol{u}, \quad \boldsymbol{\omega}^{(u)}(\boldsymbol{x}) \approx \boldsymbol{N}_u \boldsymbol{\omega}^{(u)} \tag{19b}$$

where $\boldsymbol{N}_T$ and $\boldsymbol{N}_u$ are the matrices of shape functions for the temperature and displacement, respectively; $\boldsymbol{T}$ and $\boldsymbol{u}$ are the matrices of nodal temperature and displacement, respectively; $\boldsymbol{\omega}^{(T)}$ and $\boldsymbol{\omega}^{(u)}$ are the matrices of the nodal values for the weight functions.

The weak forms given in Eqs. (6) and (10) are integrated over all finite elements, yielding the following compact systems after eliminating the matrices of weight functions:

$$\boldsymbol{M}_T \boldsymbol{T} = \boldsymbol{R}_T \tag{20a}$$

$$\boldsymbol{M}_u \boldsymbol{u} = \boldsymbol{R}_u \tag{20b}$$

with

$$\boldsymbol{M}_T = \int_\Omega (\frac{\rho c}{\Delta t} \boldsymbol{N}_T^T \boldsymbol{N}_T + \boldsymbol{B}_T^T \boldsymbol{K} \boldsymbol{B}_T) \mathrm{d}\Omega \tag{21a}$$

$$\boldsymbol{R}_T = \int_\Omega \boldsymbol{N}_T (\boldsymbol{Q} + \frac{\rho c}{\Delta t} \boldsymbol{T}^{(0)}) \mathrm{d}\Omega - \int_{\Gamma_q} \boldsymbol{N}_T^T \bar{\boldsymbol{q}} \mathrm{d}\Gamma \tag{21b}$$

$$\boldsymbol{M}_u = \int_\Omega \boldsymbol{B}_u^T \boldsymbol{D} \boldsymbol{B}_u \mathrm{d}\Omega \tag{21c}$$

$$\boldsymbol{R}_u = \int_\Omega \rho \boldsymbol{N}_u^T \boldsymbol{b} \mathrm{d}\Omega - \int_\Omega \boldsymbol{B}_u^T \boldsymbol{\sigma}^{(0)} \mathrm{d}\Omega + \int_{\Gamma_t} \boldsymbol{N}_u^T \bar{\boldsymbol{t}} \mathrm{d}\Gamma_t \tag{21d}$$

where $\boldsymbol{K}$ is the matrix of thermal conductivity; $\boldsymbol{T}^{(0)}$ is the matrix of initial nodal temperature for a steady state; $\boldsymbol{\sigma}^{(0)}$ is the matrix of stress before applying nodal displacement $\boldsymbol{u}$ to the domain; $\boldsymbol{D}$ is the matrix of stiffness given in Eq. (18); $\boldsymbol{B}_T$ and $\boldsymbol{B}_u$ are the matrices of derivatives of shape functions for the temperature and displacement fields, respectively. Note that all matrices in the two compact systems are assembled at the global level. It is straightforward to solve the linear system of the thermal conduction given in Eq. (20a), whilst the mechanical response given in Eq. (20b) is non-linear and needs iterative solutions due to the dependence of stiffness matrix $\boldsymbol{M}_u$ on the nodal

displacement $\boldsymbol{u}$. The Newton–Raphson method is utilized to solve Eq. (20b) with a convergence criterion

$$\frac{\|\boldsymbol{R}_u\|_2}{\|\boldsymbol{R}_u^{(0)}\|_2} \leq \epsilon_f \tag{22}$$

where ϵ_f is the relative residual of the mechanical system; $\boldsymbol{R}_u^{(0)}$ is the initial residual force before applying nodal displacement $\boldsymbol{u}$ to the domain; $\| \bullet \|_2$ denotes the L2-norm.

2.3.2. DEM solver

The Gauss quadrature is applied to the numerical integration (see Eq. (21)a-d) in the two concurrent FEM solvers. In the hierarchical approach, the conventional phenomenological constitutive relation is no longer needed, which can be, however, directly extracted from the DEM solver. That is to say, the homogenized response of a DEM assembly (i.e., an RVE) composed of finite discrete particles serves as the response at each Gauss (quadrature) point. Hence, the thermal conductivity matrix $\boldsymbol{K}$ in Eq. (21)a and the stiffness matrix $\boldsymbol{D}$ in Eq. (21)c can be assembled in terms of the thermal conductivity tensor in Eq. (13) and the tangent operator in Eq. (18) over all DEM assemblies at all Gauss points, respectively. For the sake of implementation without loss of generality, regular-shape (parallelogram in 2D, parallelepiped in 3D) RVE assemblies with periodic boundaries are employed as in the literature [32]. Note that each Gauss point has only one temperature so that the RVE assembly is exposed to an isothermal field, hereby there is no need to model thermal conduction through the assembly. Nevertheless, the mechanically-induced change in thermal conductivity needs to be taken into account [55].

In DEM, particles iteratively update their states (positions, velocities and accelerations) by the Newton's law with an explicit integration scheme, on which the detail of the background theory is not presented here for brevity but referring to the literature [56] for interested readers. For a thermal–mechanical problem, the RVE assembly at each Gauss point experiences both temperature variation and mechanical deformation. The temperature variation results in the corresponding variation in particle size by Eq. (16) accordingly, and the accompanying thermally-induced force is seamlessly embedded into the inter-particle force in Eq. (14). Meanwhile, with the deformation gradient $u_{i,j}$, the RVE assembly is deformed according to the strain $\epsilon_{ij}(= (u_{i,j} + u_{j,i})/2)$ and the rigid body rotation $w_{ij}(= u_{i,j} - \epsilon_{ij})$, and then the thermal conductivity tensor, the stress tensor and the tangent operator are obtained by Eqs. (13), (17) and (18), respectively.

2.3.3. Coupling scheme

Fig. 2 summarizes the hierarchical coupling approach of the two concurrent FEMs and the DEM for thermo-mechanical modeling, according to the following steps:

(1) Establishing two superposed FEM meshes (with shared nodes and Gauss points) for thermal and mechanical solvers;
(2) Attaching an RVE assembly to each Gauss point shared by the two superposed meshes;
(3) Traversing all Gauss points, and obtaining the initial temperature $\boldsymbol{T}^{(0)}$, thermal conductivity $\boldsymbol{K}$, stress $\boldsymbol{\sigma}^{(0)}$, and tangent operator $\boldsymbol{D}$ from all RVE assemblies;
(4) Solving the thermal system in Eq. (20a) and obtaining the updated temperature for each Gauss point;
(5) Solving the mechanical system in Eq. (20b) and obtaining the deformation gradient for each Gauss point;
(6) Applying both deformation and thermal expansion to each RVE assembly, and obtaining the updated stress, tangent operator, and thermal conductivity tensor for each Gauss point;
(7) Going back to Step (5) until the relative residual of the mechanical system is sufficiently small ($\epsilon_f = 0.01$ in Eq. (22) in this study).

The open-source FEM code *Esys-Escript* [57] is employed to serve as the two (thermal and mechanical) FEM solvers at the macroscopic scale. The microscopic thermo-mechanical model for non-spherical particles is implemented in our open-source code *SudoDEM* [40,47]. *SudoDEM* is developed explicitly for DEM modeling of non-spherical particles, which provides a rich of particle shapes such as superellipsoids, poly-superellipsoids, polyhedrons, cylinders and cones for 3D, and disks, superellipses for 2D. For example, the profile of a superelliptic particle as shown in Fig. 2 can be given by

$$\left|\frac{x}{r_x}\right|^{\frac{2}{\epsilon}} + \left|\frac{y}{r_y}\right|^{\frac{2}{\epsilon}} = 1 \tag{23}$$

FEM Solvers
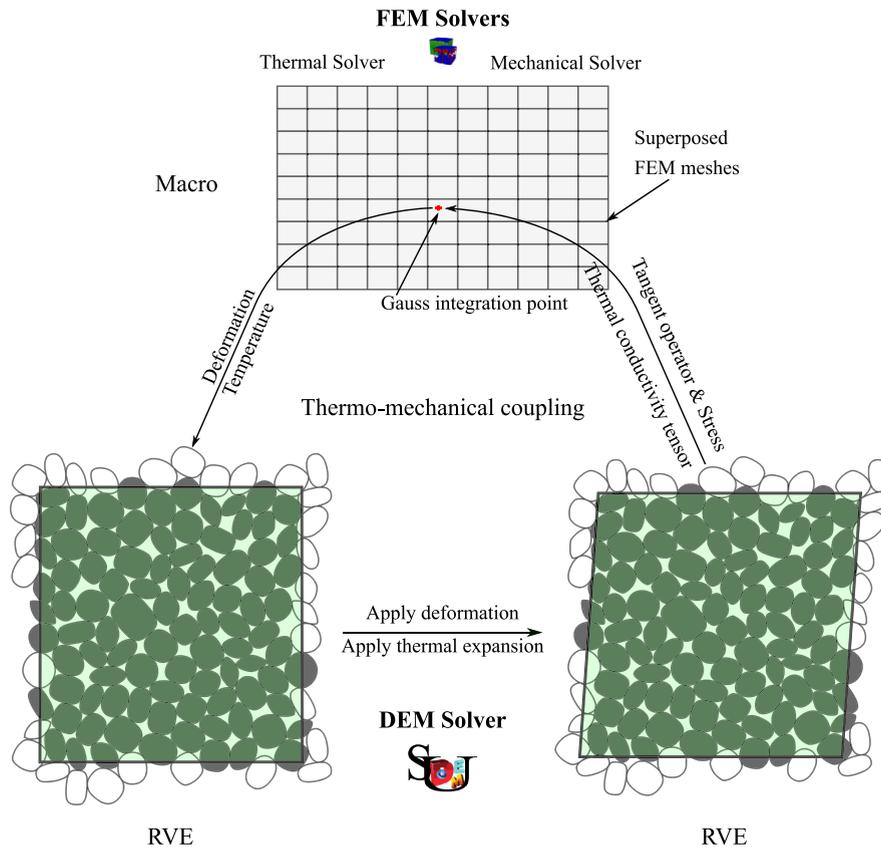
Fig. 2. Illustration of the solution procedure for hierarchical multiscale modeling of thermo-mechanical response in granular media. Note: particles in RVE packings are modeled by superellipses for considering the effect of particle shape.

where r_x and r_y are referred to as the semi-major axis lengths in the direction of x and y axes, respectively; ϵ is for the surface squareness. It is noteworthy that the proposed thermo-mechanical coupling framework is general and robust and can be applied to any grain shapes. The specific implementation and calculation of thermally-induced contact forces, however, might vary for different particle shapes. For example, for the non-spherical shapes with explicit principal axes (e.g., superellipsoids, poly-superellipsoids, and superellipses), as exemplified by superellipses in Eq. (23), the principal axis length R_i in Eq. (16) takes the semi-major axis length. In contrast, for grain shapes without explicit principal axes, e.g., polyhedrons, the distance between the ith vertex and the center of mass can be taken as R_i.

2.3.4. Computational aspects

The proposed approach records the history of all RVEs during the course of a simulation. Therefore, the DEM solver may become dominant in the usage of computer memory, which may potentially limit the solvable problem size. Hence, it is instructive to provide a quick calculation of the usage of computer memory for a double-precision floating-point computation as follows. For a two-dimensional simulation, there are three degrees of freedom (2 for translation x and y, and 1 for rotation w) for a single particle which needs 112 bytes to store information about particle shape (3 parameters for a superellipse, 24 bytes), mass (8 bytes), moment of inertia (8 bytes), position (16 bytes), orientation (8 bytes), translational and rotational velocities (24 bytes), and the resultant body force and torque (24 bytes). As for inter-particle contact, we have vector measures including contact point, contact normal, tangential vector, normal and tangential contact forces, tangential contact force at the previous time step ($6 \times 2 \times 8 = 96$ bytes), and scalar measures including contact penetration depth, and orientation of the tangent plane at the previous time step ($2 \times 8 = 16$ bytes). The storage of material properties is negligible here due to its independence of the

problem size. In addition, given an N-particle system with a mean coordination number of 10, the contact number is half of the particle number (i.e., $10 \times N/2 = 5N$) due to two particles sharing a contact. Therefore, the total usage of computer memory for both particles and contacts is $112N + 112 \times 5N = 672N$ bytes. For 1 GB (gibibytes) of RAM, the maximum particle number is 1 GB / 672 bytes $\approx 1\,597\,830$. As reported in our previous study, reliable results can be achieved with 400 particles for each RVE. If we choose 400 particles for each RVE, then we have $3\,994$ RVEs (Gauss points). Accordingly, 998 quadrilateral elements with 8 nodes and 4 Gauss points each can be handled per GB of RAM. Note that we have not considered in the above rough calculation the memory alignment in C/C++ programming, which does not introduce a significant deviation.

A physical test is performed on a thick-walled hollow disk with the same configuration in Section 3.2 but a much finer mesh ($6\,400$ quadrilateral elements). The memory usage is examined by using the command *top* on Linux. The FEM and DEM solvers take memory usage of 0.112 and 7.024 GB, respectively, where the DEM solver apparently dominates the memory usage. Moreover, there are $6\,400 \times 4 \times 400 = 10\,240\,000$ particles in total, i.e., $1\,457\,858$ particles and 911 quadrilateral elements per GB of RAM, which are close to the theoretical results. To sum up, the proposed approach is not significantly memory-demanding. Indeed, in lights of the nature of asynchronization of inter-RVE computation, the history of RVEs can be temporally dumped into a disk file, which is a possible way to reduce the cost of computer memory when the simulation scale is excessively large.

3. Benchmark

In this section, we present two benchmark examples, including transient thermal conduction and steady-state thermal conduction, to verify the proposed multi-scale modeling framework of thermo-mechanical coupling.

3.1. One-dimensional transient thermal conduction

Considering a bar with temperature and displacement fixed at both ends, as shown in Fig. 3(a), the governing equation of thermal conduction i.e., Eq. (1), is simplified by assuming no heat source ($Q_t = 0$) and $\frac{k}{\rho c} = 1$, given as

$$\frac{\partial T}{\partial t} = \frac{\partial^2 T}{\partial x^2} \quad 0 \leq x \leq L \tag{24}$$

with boundary and initial conditions

$$T(0, t) = T_1 \tag{25a}$$
$$T(L, t) = T_2 \tag{25b}$$
$$T(x, 0) = T_0 \tag{25c}$$

In this benchmark example, we focus on two special cases: for Case 1, heating at the right end with reference temperature fixed at the left end, i.e., $T_1 = T_0 = 0$ °C and $T_2 = 100$ °C; and for Case 2, heating at both ends with equal temperature i.e., $T_1 = T_2 = 100$ °C. Therefore, it is ready to deduce the analytical temperature distribution along the bar as

$$T(x, t) = \frac{T_2}{L} x + \frac{2T_2}{\pi} \sum_{n=0}^{\infty} \frac{1}{2n+1} e^{-(\frac{(2n+1)\pi}{L})^2 t} \sin(\frac{(2n+1)\pi x}{L}) \quad \text{for Case 1,} \tag{26a}$$

$$T(x, t) = T_1 - \frac{4T_1}{\pi} \sum_{n=1}^{\infty} \frac{(-1)^n}{n} e^{-(\frac{n\pi}{L})^2 t} \sin(\frac{n\pi x}{L}) \quad \text{for Case 2.} \tag{26b}$$

Then, the analytical solutions of axial stress $\sigma_x(x, t)$ and displacement $u(x, t)$ can be obtained by the following integration:

$$\sigma_x(x, t) = K_x \frac{1}{L} \int_0^L \beta T(x, t) dx \tag{27a}$$

$$u(x, t) = \beta \int_0^x T(x, t) dx - \frac{\beta x}{L} \int_0^L T(x, t) dx \tag{27b}$$
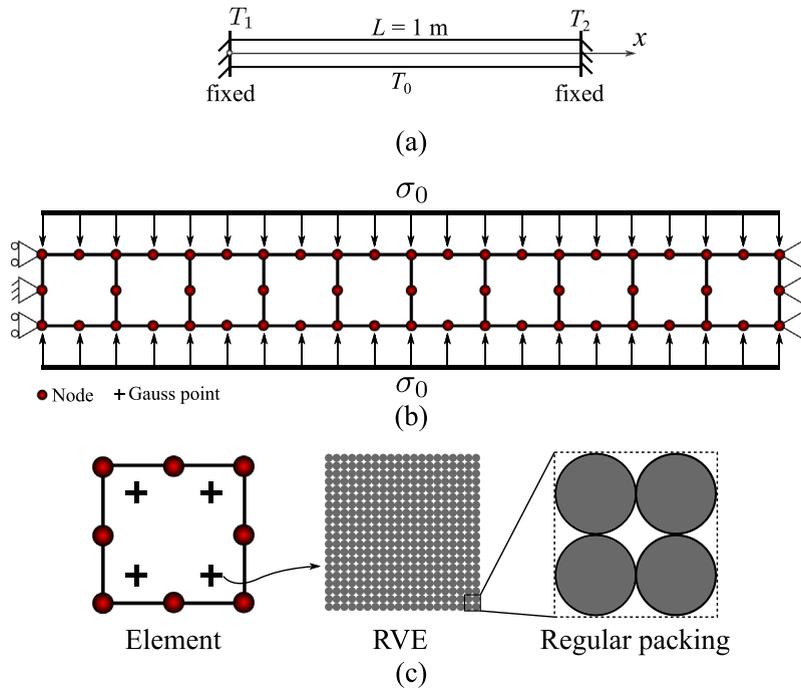
Fig. 3. (a) A simplified granular bar; (b) mesh and boundary conditions; (c) element and RVE with regular packing of disks.

where β is the linear thermal expansion coefficient; K_x is the stiffness along the bar, which can be estimated from the first component of the stiffness matrix, i.e., D_{1111} for 2D.

The simulation setup is shown in Fig. 3(b). The bar is uniformly discretized into ten-by-one quadrilateral elements with a dimension of 0.1 m $\times$ 0.1 m for each, and a constant confining stress σ_0 of 100 kPa is applied to the upper and lower sides. Each quadrilateral element has 8 nodes and 4 Gauss (quadrature) points, as shown in Fig. 3(c). Identical RVE packings with periodic boundaries are then attached at each Gauss point after consolidation (isotropic compression) with a confining stress of 100 kPa. The detail on the consolidation of the RVE packing is not presented here for brevity, and interested readers are referred to the conventional procedures for DEM simulations in the literature [48,58]. Moreover, given that the focus is on the response along the bar, a regular (simple cubic) packing of 400 mono-sized disks (with radius $r = 5$ mm) is employed to maintain a changeless configuration, thereby ensuring an almost invariant bulk elasticity parameter (i.e., K_x as introduced in Eq. (27)) for a better comparison with the analytical solutions. Besides, the imagined third dimension z_p for the 2D RVE packing is set to 25 times of particle radius, which serves to calculate the RVE volume involved in the computation of stress and stiffness tensors (see Eqs. (17)–(18)). It is worth noting that z_p is not a magic number, which, however, should be sufficiently small to avoid significantly large magnitudes of inter-particle contact forces which in turn demands the use of high contact stiffness values to ensure small overlap between particles. Furthermore, the material properties of particles are selected in experience as follows: the density of solid $\rho_s = 2650$ kg/m^3, the contact stiffness $k_n = k_t = 1 \times 10^6$ N/m, the coefficient of friction $\mu = 0.001$, and the linear thermal expansion coefficient $\beta = 1 \times 10^{-4}$/K. The particles are assumed almost frictionless to ensure relatively small deviations in the material properties (e.g., Young's modulus) among all RVEs during the simulation, thereby rendering it reasonable to use constant material properties in the analytical solutions. These selected parameter values will be used in all remaining simulations unless otherwise stated. Note that these selected parameters need careful calibration (e.g., by using the Bayesian filtering approach [59]) if one wants to obtain comparable numerical results with the experimental one. We also note that the gravitational force is not considered in the quasistatic simulations due to negligible inertia effects.

The time step is set to 0.01 s in terms of Eq. (7) for the integration of the transient thermal conduction for both cases. The distributions of temperature and displacement at different times are shown in Fig. 4 for the two
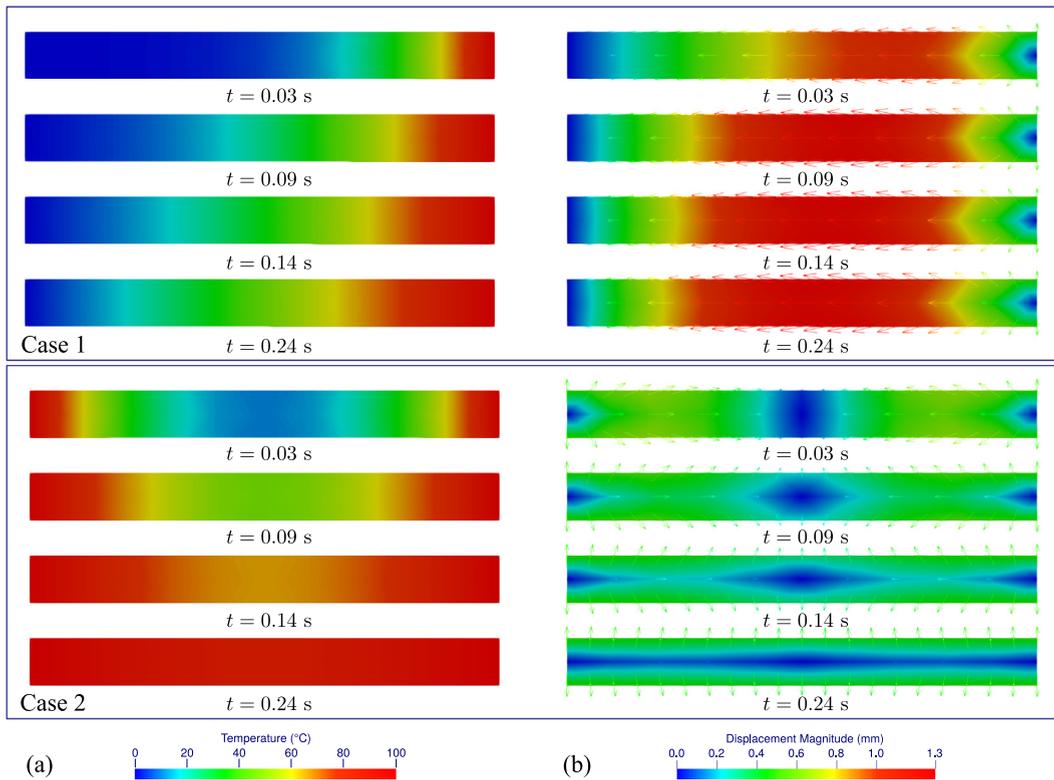
Fig. 4. Temperature (a) and displacement (b) distributions for the two cases at different times.
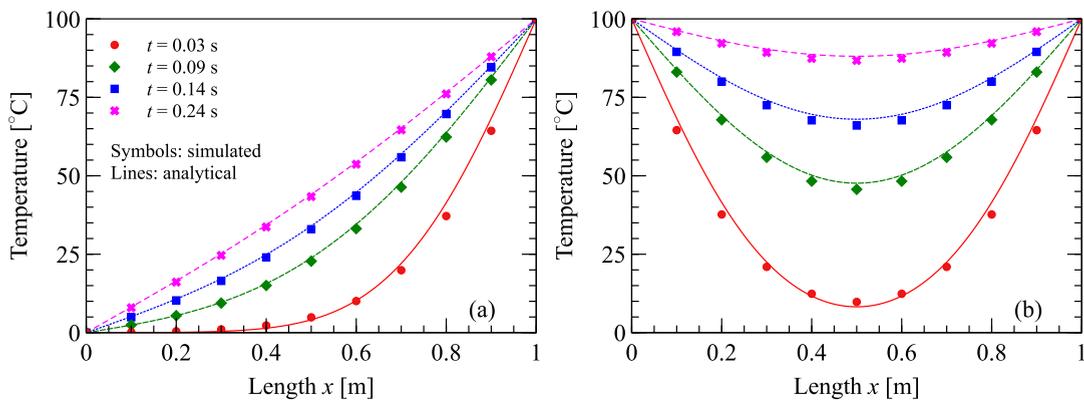
Fig. 5. Comparison between simulated and analytical results of temperature for (a) Case 1, (b) Case 2.

cases. Qualitatively, for Case 1, both the temperature and the displacement gradually increase along the bar from right to left; for Case 2, the temperature gradually increases from both ends to the middle, while the displacement decreases with thermal conduction. For a quantitative comparison with the analytical solutions, the temperature and displacement distributions at different times are plotted in Figs. 5 and 6, respectively, in which solid symbols denote the simulated results, and solid lines are for the analytical solutions. It can be seen that the results from simulations are in good agreement with the analytical solutions for both temperature and displacement in the two cases. However, one may find that the simulated displacement is, to some degree, under-estimated at the initial stage (i.e., $t = 0.03$ s in the plot) compared with the analytical one. A possible reason is that the boundary effect of fixed displacement at both ends is amplified due to coarse meshes used in the model. In addition, the evolution of axial
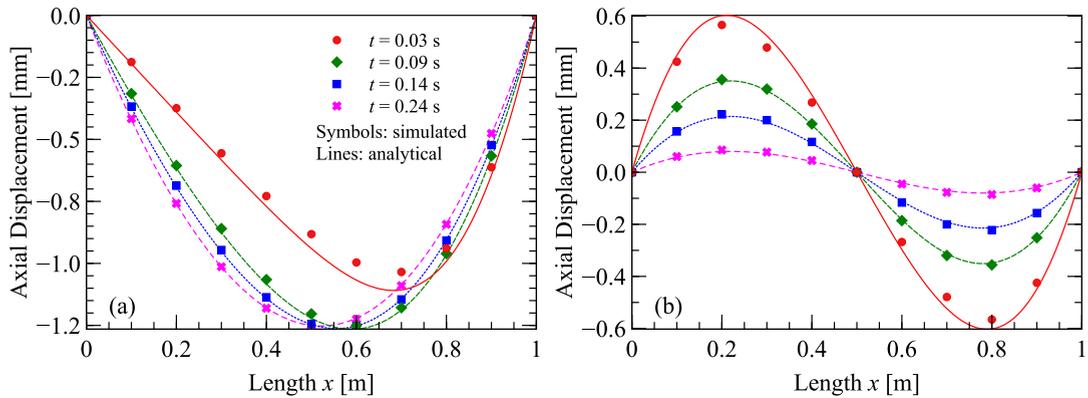
Fig. 6. Comparison between simulated and analytical results of displacement for (a) Case 1, (b) Case 2.
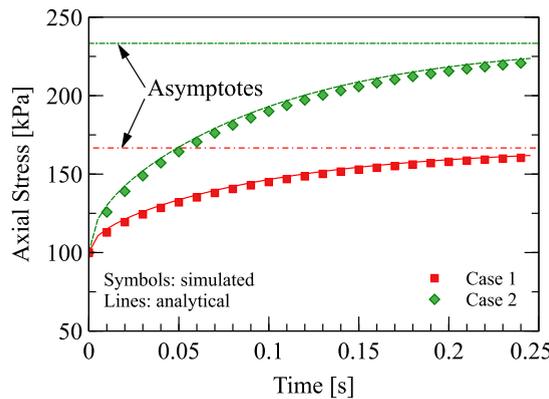
Fig. 7. Comparison between simulated and analytical results of axial stress for 1D thermal conduction in a granular bar. The asymptote lines indicate the maximum axial stress that can be reached at the final steady state of the thermal conduction.

stress for the two cases is plotted against time in Fig. 7. It is clear that the simulated and analytical results agree well with each other. Moreover, the thermally-induced stress increases as expected with increasing temperature. The maximum thermally-induced axial stress (i.e., the asymptote excluding the prescribed stress 100 kPa) that can be reached for Case 2 is twice as high as that for Case 1.

3.2. Two-dimensional steady-state thermal conduction

In this benchmark example, we examine the thermal conduction and its thermally-induced stress within a thick-walled hollow disk with inner and outer radii $r_0 = 0.5$ m and $r_1 = 5.0$ m, respectively. A constant pressure (or confining stress) σ_0 of 20 kPa is applied to both inner and outer surfaces. The inner surface of the thick-walled disk is exposed to a temperature increase of T_0, while the temperature T_1 at the outer surface maintains 0 °C. Therefore, with the assumption that the thermal and mechanical properties are homogeneous, the temperature profile across the thickness at the steady state is given as [60]

$$T(r) = \frac{T_0}{\ln \frac{r_1}{r_0}} \ln \frac{r_1}{r} \tag{28}$$

where r is the distance from the center of the thick-walled disk. Accordingly, the stress can be deduced by superposing the initial stress σ_0 and the thermally-induced stress, i.e.,

$$\sigma_r = \frac{E\beta T_0}{2r^2 \ln \frac{r_1}{r_0}} \Big[\frac{(r^2 - r_1^2) r_0^2}{r_1^2 - r_0^2} \ln \frac{r_0}{r_1} + r^2 \ln \frac{r}{r_1} \Big] + \sigma_0 \tag{29a}$$
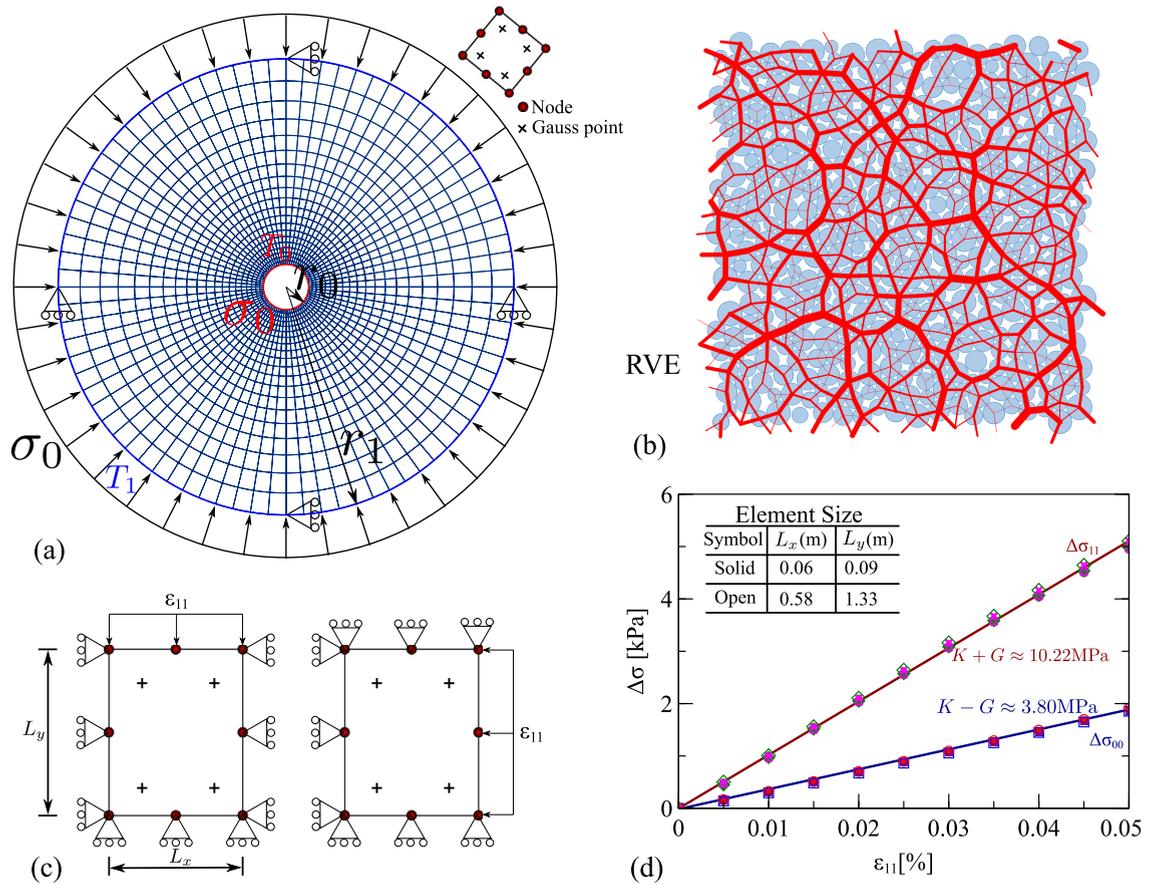
Fig. 8. (a) Mesh and boundary conditions for the thicked-wall disk; (b) RVE packing of disks with a confining stress of σ_0; (c) boundary conditions for one-dimensional compression at the top (*left*) or the right (*right*) of a single element; (d) elasticity parameters of the bulk granular assembly at small strains from the test in (c) with the largest and smallest element sizes of (a).

$$\sigma_\theta = \frac{E\beta T_0}{2r^2 \ln\frac{r_1}{r_0}}\Big[\frac{(r^2 + r_1^2)r_0^2}{r_1^2 - r_0^2}\ln\frac{r_0}{r_1} + r^2\ln\frac{r}{r_1} + r^2\Big] + \sigma_0 \tag{29b}$$

$$\sigma_{r\theta} = 0 \tag{29c}$$

where σ_r, σ_θ and $\sigma_{r\theta}$ are radial, tangential, and shear stresses, respectively; E is the Young's modulus, and β is the linear thermal expansion coefficient.

The open-source mesh generator *Gmsh* [61] is utilized to generate 400 unevenly distributed eight-node quadrilateral elements. The mesh and boundary conditions for the domain are shown in Fig. 8(a). In this example, the RVE is almost homogeneous random packing of disks with radius uniformly between 2.5 and 5.0 mm (the potential effect of particle size distribution on packing [62] is not considered here without loss of generality), referring to Fig. 8(b), whose elasticity parameters such as the bulk modulus K and the shear modulus G are estimated from one-dimensional compression tests on a single element. Fig. 8(c) shows the boundary conditions of the element tests with two specific loading directions (i.e., along the vertical and the horizontal) for considering the possible deviation from the intrinsic anisotropy of the RVE packing. In addition, we also take into account two element sizes 0.06 m × 0.09 m and 0.58 m × 1.33 m, corresponding to the finest and the coarsest elements, respectively, in the domain of the thick-walled disk. The small-strain mechanical responses of the total four element-tests are shown in Fig. 8(d), where the stress–strain lines offer the following relations: $\Delta\sigma_{11}/\Delta\epsilon_{11} = K + G$ and $\Delta\sigma_{00}/\Delta\epsilon_{11} = K - G$ in 2D. Note that the deviation of the four stress–strain slopes is negligibly small, indicating that the prepared RVE
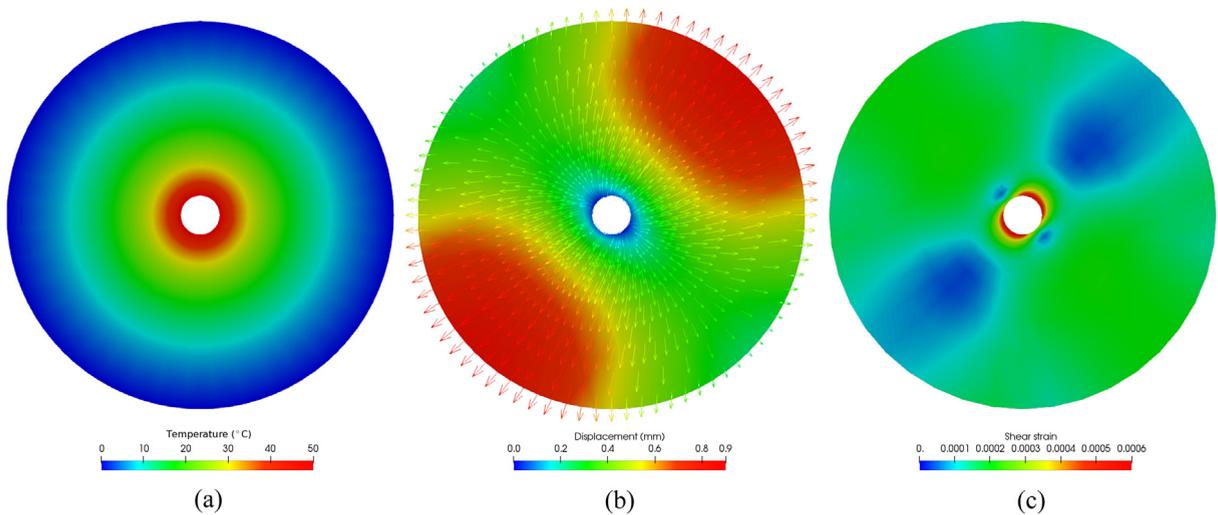
Fig. 9. Temperature (a), displacement (b) and shear strain (c) distributions at $T_0 = 50$ °C.

packing is sufficiently homogeneous. Finally, the Poisson's ratio is given as $\nu = (K - G)/(K + G) \approx 0.372$, and the Young's modulus reads as $E = 2K(1 - \nu) \approx 8.8$ MPa in 2D [63].

Three simulations are carried out with inner temperature $T_0 = 10$, 25, and 50 °C, respectively. Fig. 9 shows the distributions of temperature, displacement, and shear strain within the thick-walled disk for $T_0 = 50$ °C. As expected, the temperature decreases gradually and symmetrically from inner to outer surfaces in Fig. 9(a), meanwhile, as shown in Fig. 9(b), the thick-walled disk expands radially outward nearly symmetrically. It is clear that the displacement distributes not as symmetrically as the temperature does, which is, however, not surprising due to the internal anisotropy of granular materials. Indeed, shear-induced anisotropy can be significant in granular materials [15,64]. Nevertheless, the thermal perturbation is deliberately restrained small by a moderate temperature T_0 to ensure only weak shear occurring so that a constant Young's modulus still works for the analytical solutions given in Eq. (29). As can be seen in Fig. 9(c), the maximum shear strain (approximately 0.0006) locates at the inner surface for the given problem, which is indeed negligibly small.

Fig. 10(a) shows that the simulated temperature profile is consistent with the analytical one given by Eq. (28) for all the three inner temperatures. As for the stress within the thick-walled disk, we extract the stress state ($\sigma_{xx}, \sigma_{xy}, \sigma_{yy}$ in the Cartesian coordinate system) at each Gauss point and transfer it to the polar coordinate system with the following relationship

$$\sigma_r = \cos^2\theta\sigma_{xx} + 2\sin\theta\cos\theta\sigma_{xy} + \sin^2\theta\sigma_{yy} \tag{30a}$$

$$\sigma_\theta = \sin^2\theta\sigma_{xx} - 2\sin\theta\cos\theta\sigma_{xy} + \cos^2\theta\sigma_{yy} \tag{30b}$$

$$\sigma_{r\theta} = \sin\theta\cos\theta(\sigma_{yy} - \sigma_{xx}) + (\cos^2\theta - \sin^2\theta)\sigma_{xy} \tag{30c}$$

where θ is the angular direction. Then, averaging the stress over all θ at the same radial distance r yields the simulated radial, tangential, and shear stresses ($\sigma_r, \sigma_\theta, \sigma_{r\theta}$), which are plotted together with the analytical solutions given by Eq. (29) in Figs. 10(b), (c) and (d), respectively. The radial stress σ_r increases to reach a peak at a distance of approximately $2r_0$, then decreases to the initial stress at the outer surface. By contrast, the tangential stress σ_θ experiences a monotonic decrease with radial distance r increasing, and a stationary point (where $\sigma_\theta = \sigma_0$) appears at a distance of approximate $4.5r_0$. Moreover, it is of interest to see two different trends for the radial and tangential stresses with inner temperature T_0 increasing: the radial stress σ_r increases for all points through the thickness, while the tangential stress σ_θ increases at the left of the stationary point but decreases at the other side. The simulated shear stress $\sigma_{r\theta}$ is negligibly small (less than 1 Pa) and can be regarded as zero, compared with the initial stress σ_0 of 20 kPa. Furthermore, one finds that the stress near the inner surface has a moderate deviation between the simulated and analytical results, especially for $T_0 = 50$ °C, and the deviation is likely to become more significant with increasing T_0. A reasonable explanation is that significantly inhomogeneous shear takes place near the inner
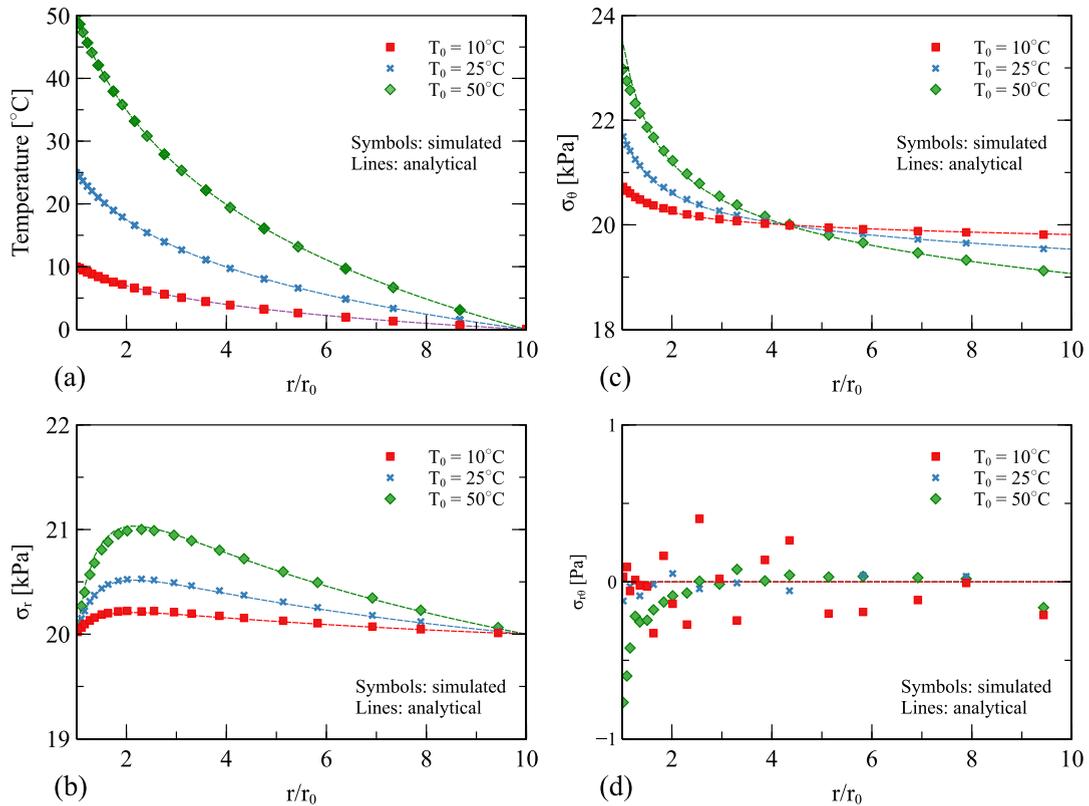
Fig. 10. Profiles of temperature (a), radial stress (b), tangential stress (c) and shear stress (d) throughout the thickness of the thick-walled disk for the three different inner temperatures.

surface as aforementioned (see Fig. 9(c)) so that the homogeneous assumption fails in deducing the analytical solution. Overall, the simulated stress is consistent with the analytical one.

4. Responses of confined granular columns under thermal cycling

The proposed multiscale modeling approach is further applied to investigating the response of a granular column under thermal cycling. As a demonstration, the emphasis is placed on two critical aspects of both external and internal factors, i.e., boundary condition and inherent anisotropy of the granular column.

4.1. Effect of boundary condition

Considering a 2D granular column with a dimension of 1 m × 1 m, the entire domain is discretized into 8-by-8 quadrilateral elements with 8 nodes and 4 Gauss points for each, as shown in Fig. 11, where four different combinations of thermal and mechanical boundary conditions are introduced for the thermal cycling problem. Figs. 11(a) and (b) show the constant stress (CS) boundary condition, by which the top of the domain is given a prescribed stress σ_0, while the other three sides are fixed in displacement along their corresponding outward normals. As for the constant volume (CV) boundary condition, the displacement along the outward normal of the entire boundary is fixed, as shown in Figs. 11(c) and (d). Besides, for the thermal boundary condition, a periodically varying temperature T_1 is given at the top (T) or the right (R) sides of the domain, while the other three sides maintain a reference temperature T_0. For the convenience of presentation, the four thermo-mechanical boundary conditions are denoted by CSR, CST, CVR, and CVT, respectively, as shown in Figs. 11(a-d). Moreover, at the initial state, i.e. time $t = 0$, the entire granular column situates at the reference temperature $T_0 = 0$ °C with a pre-stress of $\sigma_0 = 20$ kPa.

(a) CSR   (b) CST   (c) CVR   (d) CVT
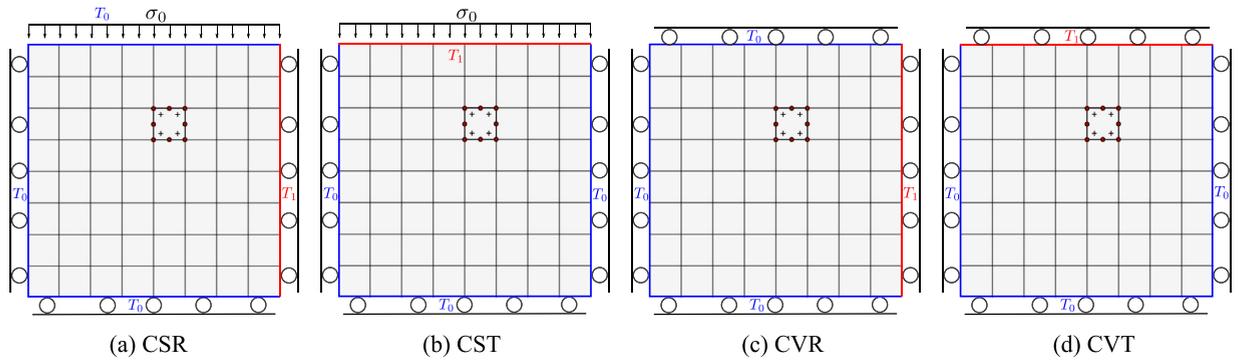
Fig. 11. Meshes and boundary conditions: constant stress with heating at the right (a) and top (b); constant volume with heating at the right (c) and top (d).

(a)   (b)   (c)
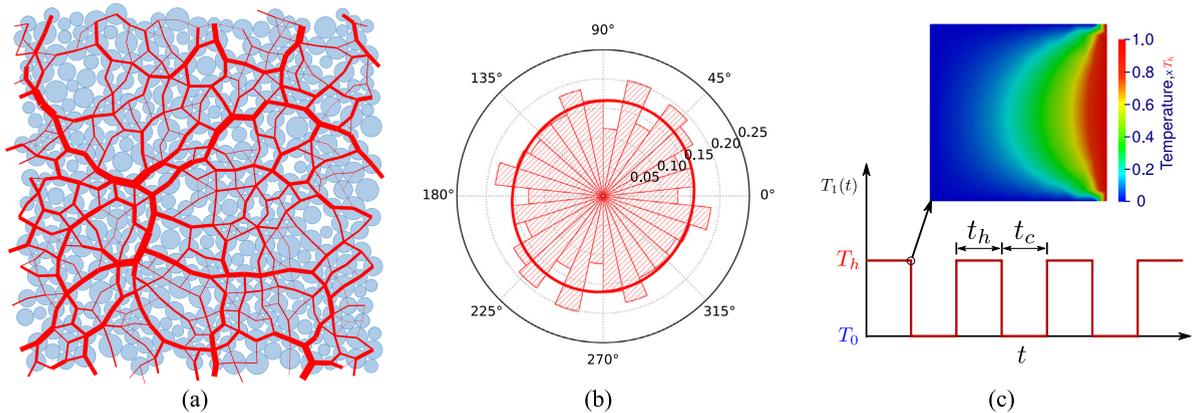
Fig. 12. (a) The initial RVE packing with contact force-chains shown in red; (b) the distribution of contact normal within the initial RVE packing where the curve is the best Fourier fitting; (c) the temperature T_1 varying with time t, where the inset is a typical contour of temperature for the case heating at the right.

The initial RVE packing of 400 disks with radii uniformly lying between 2.5 and 5.0 mm is consolidated with a confining stress $\sigma_0 = 20$ kPa, as shown in Fig. 12(a). In the preparation of the RVE packing, the inter-particle coefficient of friction μ is set to 0.5 to obtain a frictional granular system, and the other parameters remain the same as introduced in the benchmark examples (see Section 3). The distributions of contact force-chains in Fig. 12(a) and contact normal in Fig. 12(b) suggest that the RVE packing is almost isotropic from both qualitative and quantitative points of view. The RVE packing is then attached to each of the total 256 Gauss points of the domain. For simplicity, the temperature T_1 at the heating side of the granular column is assumed to vary in a square-wave manner, as shown in Fig. 12(c), in which t_h and t_c are the time intervals for heating ($T_1 = T_h = 100$ °C) and cooling ($T_1 = T_0 = 0$ °C) phases, respectively. The inset of Fig. 12(c) shows a typical contour of temperature across the granular column after heating at the right boundary. The thermal parameters are set as follows [18,50,65]. The thermal capacity of solid is selected from quartz sands $c_s = 800$ J/kg/K. The thermal resistance $\eta = 1.5 \times 10^5$ K/W/m to meet a bulk thermal conductivity of 2.4 W/m/K for sandy soils typically measured in the laboratory. The time intervals of heating and cooling $t_h = t_c = 10\Delta t_s$, where Δt_s is the time step for solving the thermal transient problem, set to 3 h here which does not exceed the estimated critical time step given by Eq. (7). Two linear thermal expansion coefficients $\beta = \beta_0$ and $\beta = 5\beta_0$ (where $\beta_0 = 1 \times 10^{-5}$/K) are considered for sensitivity analysis.

Fig. 13 shows the evolution of temperature profile along the central-horizontal slice of the right heating case (CSR) during one cycle of heating and cooling. It suggests that a 30-hour ($10\Delta t_s$) time interval (i.e., t_h, t_c) is sufficient to make heating or cooling phases reach their final steady states during thermal conduction.

The mechanical response at the interface between granular materials and structures plays an essential role in the safety design in engineering (e.g., interface-shear resistance of thermal piles [66] and other geostructures [67]) and
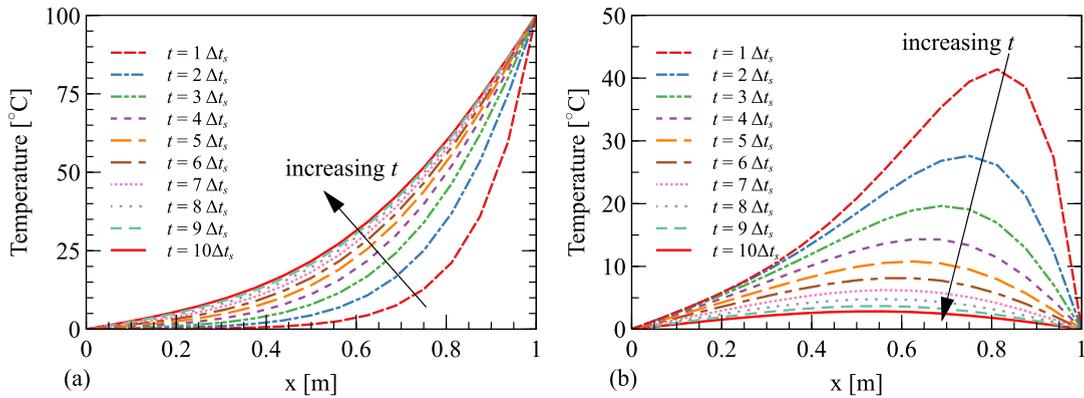
Fig. 13. Evolution of temperature profile along the central-horizontal slice of the right heating case CSR) during a single cycle of heating (a) and cooling (b) phases. The left and right boundaries of the granular column locate at $x = 0$ and 1 m, respectively.
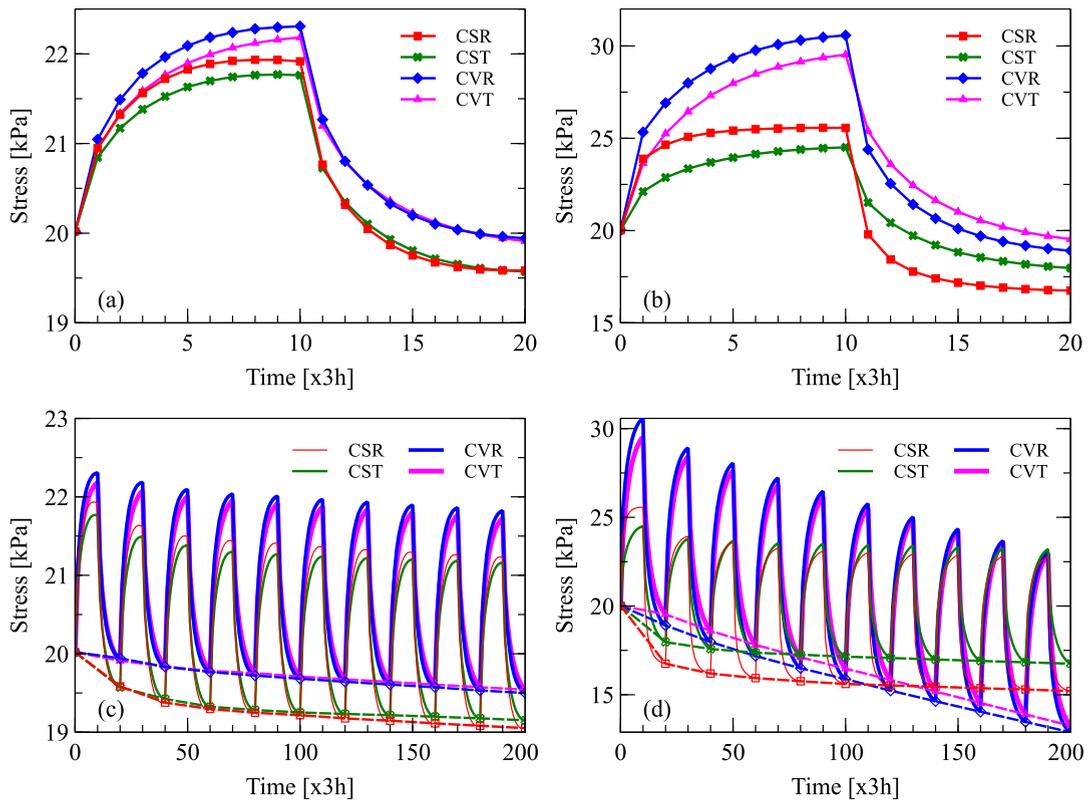
Fig. 14. Evolution of the normal stress at the right boundary (NSR) for the four cases with linear thermal expansion coefficients of β_0 (a, c) and $5\beta_0$ (b, d) during thermal cycling. The dashed lines in (c) and (d) denote the evolution at the reference temperature.

industry (e.g., strength of silos [68]). It is thus of interest to examine the thermally-induced responses (e.g., stress and displacement variation) at the boundary of the granular column. For convenience without loss of generality, only one interface is focused on, i.e., the right boundary of the domain. The normal stress at the right boundary (averaged over the boundary, hereafter referred to as NSR) is examined during the first thermal cycle, as shown in Fig. 14(a), in which NSR increases to a plateau with temperature increasing during heating, then decreases to a relatively steady value as temperature decreases during cooling. It is evident that the NSR for the constant volume boundary condition (i.e., CVR and CVT) is more significant than that for the constant stress boundary condition (i.e., CSR
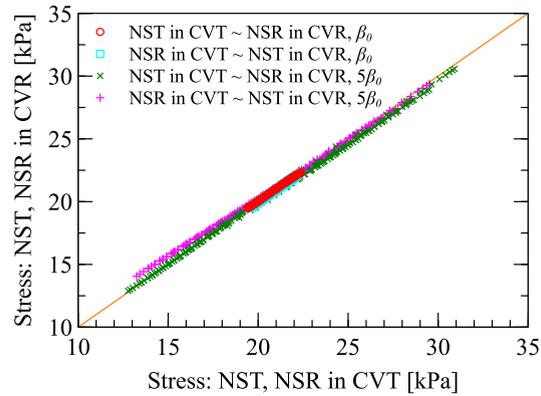
Fig. 15. The normal stresses at the right boundary (NSR) and at the top boundary (NST) of CVR and CVT with linear thermal expansion coefficients of β_0 and $5\beta_0$ during thermal cycling.

and CST) at the first thermal cycle for both heating and cooling phases. A reasonable explanation is that the constant volume constrains the plastic deformation of granular materials, thereby resulting in a higher plateau at heating and a smaller stress relaxation after cooling. Moreover, as expected, heating at the right boundary makes NSR more significant than that at the top boundary due to stronger thermal expansion in the horizontal, e.g., CSR vs. CST, and CVR vs. CVT. However, there is no significant difference in NSR between the two heating locations after cooling. A reasonable explanation is that the plastic deformation is not significant due to moderate thermal perturbation caused by the small thermal expansion coefficient. That is to say, most of the deformation during the moderate thermal cycling can be recoverable (i.e., elastic). Indeed, with a more significant thermal expansion coefficient, as shown in Fig. 14(b), heating at the right boundary yields more significant stress relaxation after cooling. Meanwhile, the thermally-induced stress is more significant compared with that for a small thermal expansion coefficient.

During thermal cycling, as shown in Figs. 14(c) and (d), NSR behaves in a wave manner with an almost constant amplitude for all the studied cases. After joining the data points sequentially at the reference temperature, referring to the dashed lines, a continuous decrease in NSR is observed. It indicates that thermal cycling can induce stress relaxation, which can become significant due to accumulative effect. Also, the stress relaxation is expected to reach a saturated point, i.e., the thermally-induced maximum relaxation, which is dominantly and positively related to the input thermal perturbation (e.g., amplitude and frequency of thermal cycling). Here it is clear that the thermal expansion coefficient is an active internal factor contributing to the thermal perturbation. As for the effect of boundary conditions, the thermal loading boundary with the thermal source experiences stronger stress relaxation. In addition, the constant volume boundary condition, to some degree, prevents the stress from dropping either for small thermal perturbation or within limited thermal cycles. However, the constant volume boundary condition can cause more significant stress relaxation than the constant stress boundary condition when the thermal perturbation is sufficiently large. Furthermore, additional attention paid to the two constant volume cases, CVR and CVT, whose boundary conditions are rotationally symmetric to each other. That is to say, the possible deviation between the response of CVR and CVT could result only from the anisotropic structures of the granular column when excluding numerical errors. Hence, the normal stress at the right boundary (NSR) from one case is plotted against that at the top boundary (NST) from the other one in Fig. 15. It is not surprising to see all data points almost locating on the line with a 1:1 slope since the RVE packing is almost isotropic (i.e., nearly without inherent anisotropy). We also point out that thermal cycling with more substantial perturbation can make particles rearrange more remarkably, thereby destroying the symmetry of fabric more severely. Thus, a more significant deviation can be seen with increasing thermal perturbation (see $5\beta_0$).

Fig. 16 shows that different boundary conditions can result in significantly distinctive patterns of displacement distribution after thermal cycling. Note that the case CVT is not presented here since its results are almost rotationally symmetric to that of CVR. For the constant stress condition, a vortex of displacement can be observed after moderate thermal cycling (see Figs. 16(a) and (b)), while the granular material flows inwards with more significant displacement after stronger thermal cycling (see Figs. 16(d) and (e)). As for the constant volume
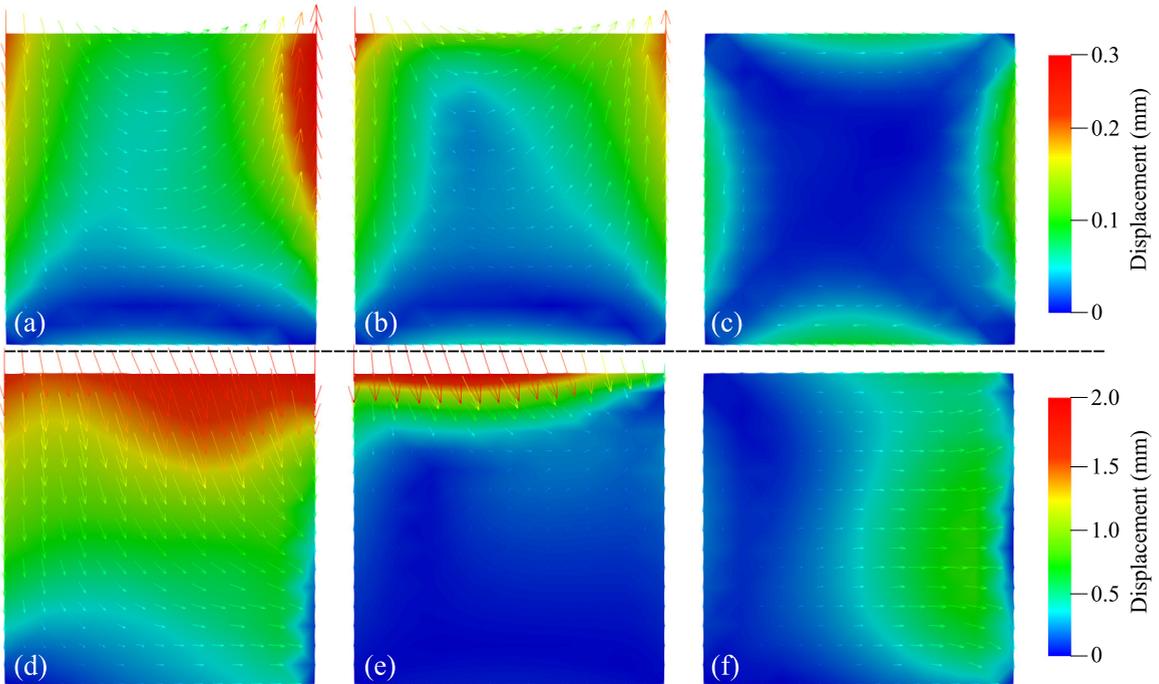
Fig. 16. Distributions of displacement for CSR (*left*), CST (*middle*) and CVR (*right*) with linear thermal expansion coefficients of β_0 (*upper*) and $5\beta_0$ (*lower*) after 10 thermal cycles.
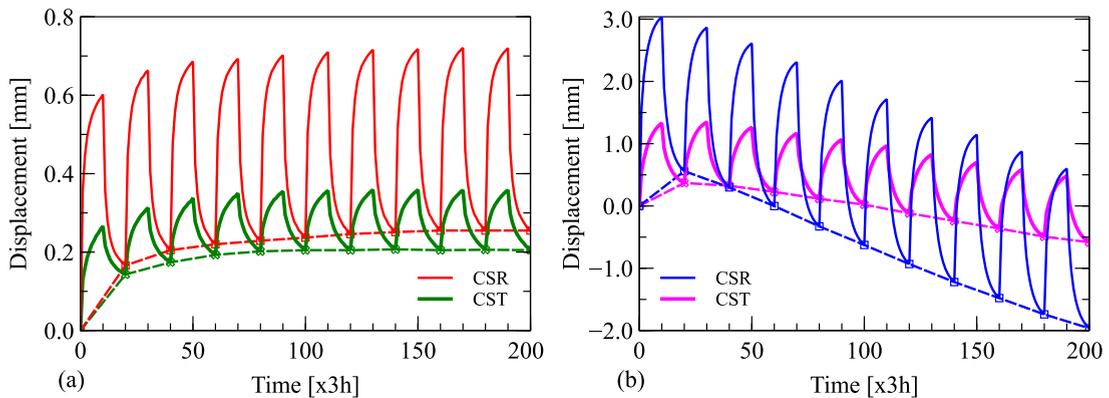
Fig. 17. Evolution of the displacement at the top-right corner for the two constant stress cases (CSR and CST) with linear thermal expansion coefficients of β_0 (a) and $5\beta_0$ (b) during thermal cycling. The dashed lines denote the evolution at the reference temperature.

condition, the granular material flows within narrow regimes near the boundary after moderate thermal cycling; however, with more vigorous thermal cycling, as shown in Fig. 16(f), the granular material notably flows towards the thermal loading boundary (i.e., the right side here). Furthermore, for the two constant stress cases, CSR and CST, it is clear that CSR experiences a stronger granular flow through the entire column than CST. Quantitatively, we plot the displacement of the top-right corner for CSR and CST during thermal cycling in Fig. 17, where the cycling amplitude of displacement in CSR is approximately 2.5 times greater than that in CST, implying a more significant thermal perturbation in CSR. Specifically, the top-right-corner displacement increases positively for moderate thermal cycling in Fig. 17(a), but the deviation in displacement for CSR and CST is not significant. With increasing thermal perturbation, i.e., $5\beta_0$ in Fig. 17(b), the top-right-corner displacement maintains a negative
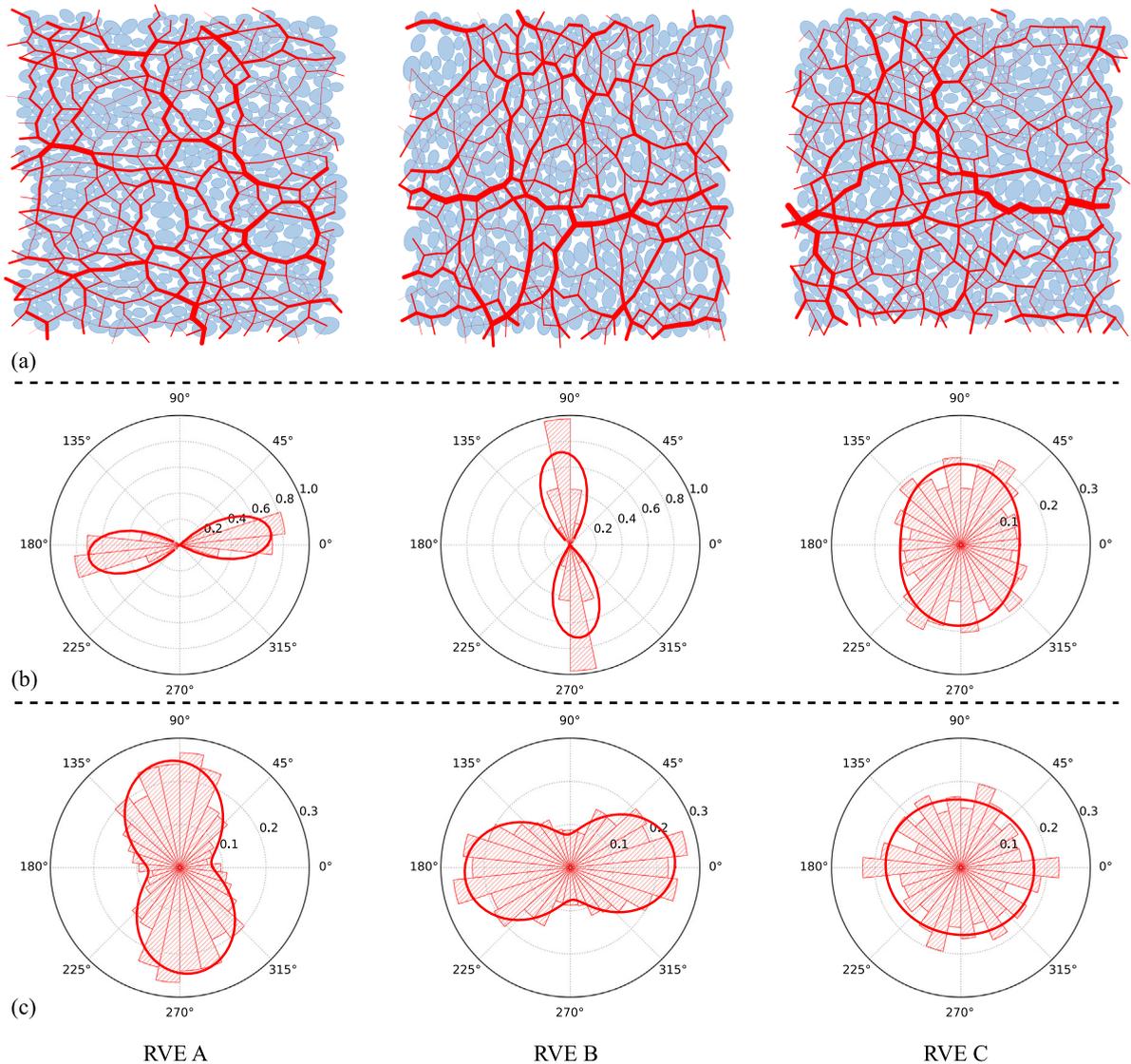
Fig. 18. Three anisotropic RVEs composed of 400 elliptic particles with an aspect ratio of 1.5: (a) packings with force-chains in red; (b) distributions of particle orientation; and (c) distributions of contact normal.

increase after the first thermal cycle, in which we can see that the displacement in CSR is more significant than that in CST.

4.2. Effect of inherent anisotropy

The inherent anisotropy of a granular material is induced by particle rearrangement during packing, which can be significantly influenced by both packing approach and properties of constituent particles, especially particle shape [39,69]. Thus, in this section, we use ellipses rather than disks to facilitate forming strong inherent anisotropy within an RVE packing. With a similar packing approach proposed in the literature [37], all particles are first fixed in rotation and confined to a medium state with a smaller confining stress (e.g., $0.5\sigma_0$), then free in rotation and consolidated to the final state with σ_0. Adjusting the confining stress at the first stage can yield final packings with different void ratios. In this way, we prepare three different RVE packings (denoted by RVE A, B, and C, respectively) with the same constituent particles and almost the same void ratio of 0.240, as shown in Fig. 18(a). Each packing consists of 400 ellipses with major semi-axis length uniformly selected between 2.5 and 5.0 mm,
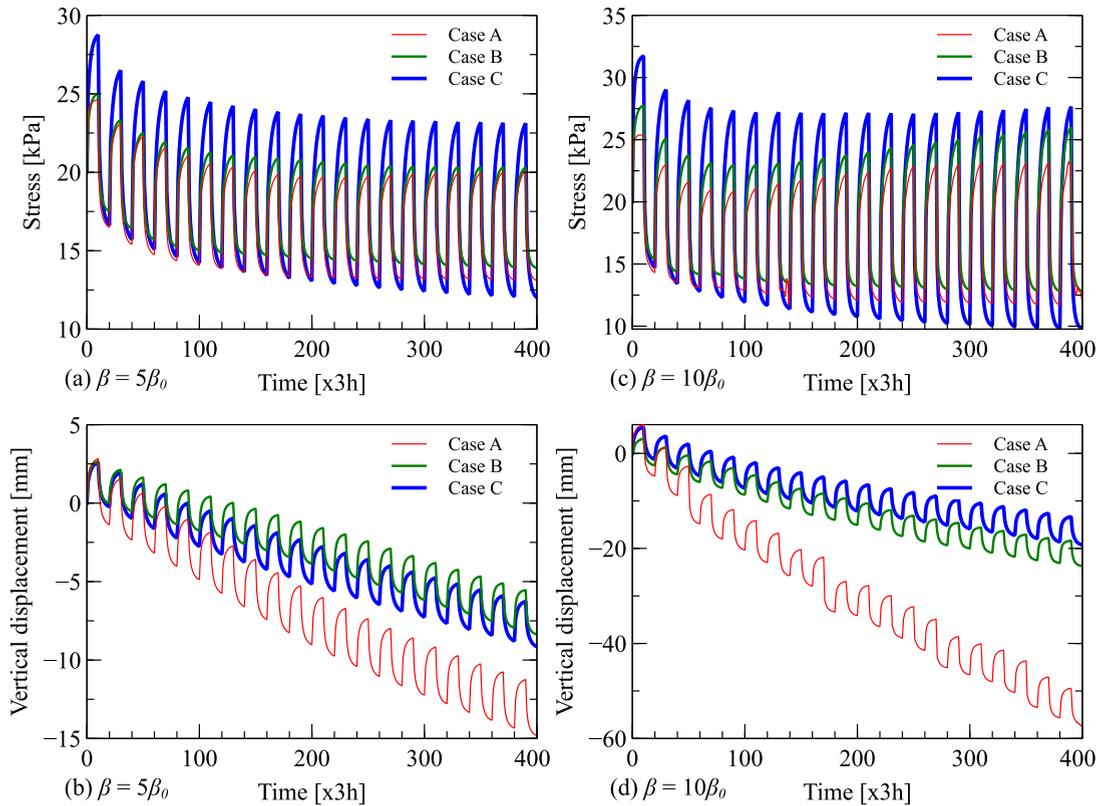
Fig. 19. Evolution of the normal stress at the right boundary (NSR) (*upper*) and the displacement at the top-right corner (*lower*) with linear thermal expansion coefficients of $5\beta_0$ (*left*) and $10\beta_0$ (*right*) during thermal cycling.

and all particles have an identical length ratio of major to minor axes (i.e., aspect ratio) of 1.5. The distributions of particle orientation (defined as the direction of the major axis) and contact normal are plotted below the corresponding packing in Fig. 18(b). It can be seen that RVEs A and B exhibit strong inherent anisotropy with most of the particles aligning in the horizontal and vertical directions, respectively, while RVE C is almost isotropic with particle orientations nearly uniformly distributed. It is also interesting to see that the distribution of contact normal has a strong correlation with that of particle orientation. For example, their major principal directions are almost orthogonal to each other. Nevertheless, we note here that this feature may not be universal for any particle shapes. Further investigation of the effect of particle shape is beyond the scope of this work. Under the same boundary condition and discretization, i.e., CSR, as introduced in Fig. 11(a), thermal cycling is performed on granular columns with the three different RVEs (RVEs A, B, and C), and the corresponding simulations are denoted by Cases A, B, and C, respectively.

Fig. 19 shows the evolution of the normal stress at the right boundary (NSR) and the displacement at the top-right corner for the three anisotropic granular columns during thermal cycling. As a general observation, the top-right-corner displacement negatively increases with stress relaxing at the boundary. With increasing thermal perturbation, i.e., increasing the thermal expansion coefficient β from $5\beta_0$ in Fig. 19(a,b) to $10\beta_0$ in Fig. 19(c,d), both the displacement and stress relaxation become more significant as aforementioned in Section 3. In addition, the inherent anisotropy plays an important role in the thermo-mechanical responses of granular materials. As shown in Fig. 19(a,c), the two considerably anisotropic granular columns Cases A and B have similar amplitudes of the thermally-induced stress during thermal cycling, but Case A has a stronger stress relaxation. Compared with Cases A and B, the almost isotropic granular column Case C has a much larger amplitude of the thermally-induced stress during thermal cycling, hereby a stronger stress relaxation. In other words, the anisotropic granular column has an enhanced resistance to stress relaxation induced by thermal cycling. This feature is analogous to the well-known fact that anisotropy enables to enhance the shear strength of granular materials subjected to external loading [15,37,64].
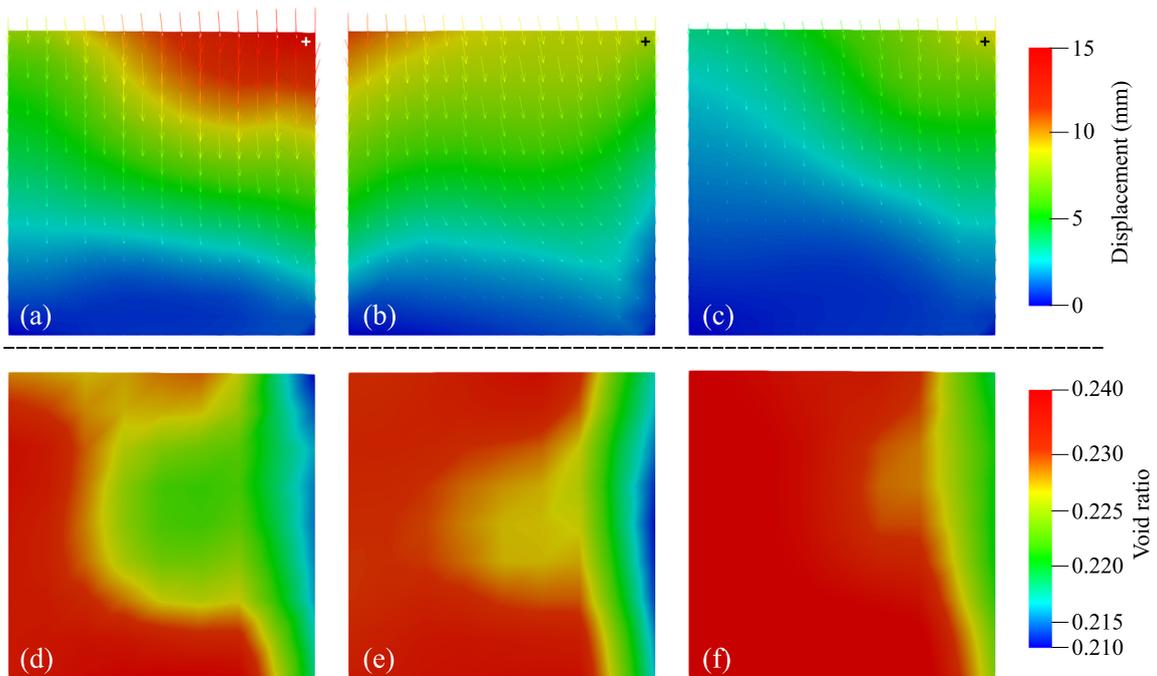
Fig. 20. Distributions of displacement (*upper*) and void ratio (*lower*) for Case A (*left*), Case B (*middle*) and Case C (*right*) with linear thermal expansion coefficient of $5\beta_0$ after 20 thermal cycles. Note: the cross symbols in (a-c) denote the Gauss points of interest at the top-right corner of the domain.

As for the thermally-induced displacement shown in Fig. 19(b,d), Case A has the most significant settlement. For the other two cases, the settlement of the top-right corner in Case C is slightly larger than that in Case B for moderate thermal perturbation in Fig. 19(b). However, Case C has the least average settlement over the displacement contour of the entire granular column, as shown in Fig. 20. All in all, thermal cycling can densify granular materials, which is in agreement with the report in both experiments and simulations [4,50,70]. Moreover, the local zone closer to the thermal loading boundary (i.e., the right boundary here) suffers from more considerable densification. To sum up, it can be concluded that the inherent anisotropy reduces the resistance of granular displacement/settlement induced by thermal cycling, and the case with particles aligning along the horizontal has the maximum settlement. Recalling the aforementioned effect of inherent anisotropy on the boundary stress, the inherent anisotropy can enhance the resistance of stress relaxation but meanwhile reduce the resistance of settlement, especially in Case A. It is worth noting that granular packing under gravity tends to the structure (the emphasis is on the inherent anisotropy) of Case A due to the major axes of particles preferring to align in the horizontal [47].

With the hierarchical coupling approach, the microscopic behavior of the granular column is available by tracking the local RVE assemblies. As a demonstration, we select the RVEs of the three granular columns at the Gauss point indicated in Fig. 20 for further analysis. The RVE assemblies of interest undergo significant thermal perturbations after thermal cycling with linear thermal expansion coefficients of $5\beta_0$ and $10\beta_0$. Their corresponding force chains and particle orientation distributions are shown in Fig. 21. Compared with the initial RVEs in Fig. 18, the force chains become more uniform and less anisotropic, and the distributions of particle orientation are less anisotropic as well. In addition, with thermal perturbation increasing (i.e., $5\beta_0$ to $10\beta_0$), the deformation performing on the RVEs is more significant, and the distributions of particle orientation become more isotropic.

5. Conclusions

We proposed a hierarchical approach based on two concurrent FEMs and DEM coupling for multiscale modeling of thermo-mechanical behavior of granular media. At the macro continuum, the quasistatic thermo-mechanical problem is split into two individual BVPs (thermal conduction and mechanical response) for thermal steady states,
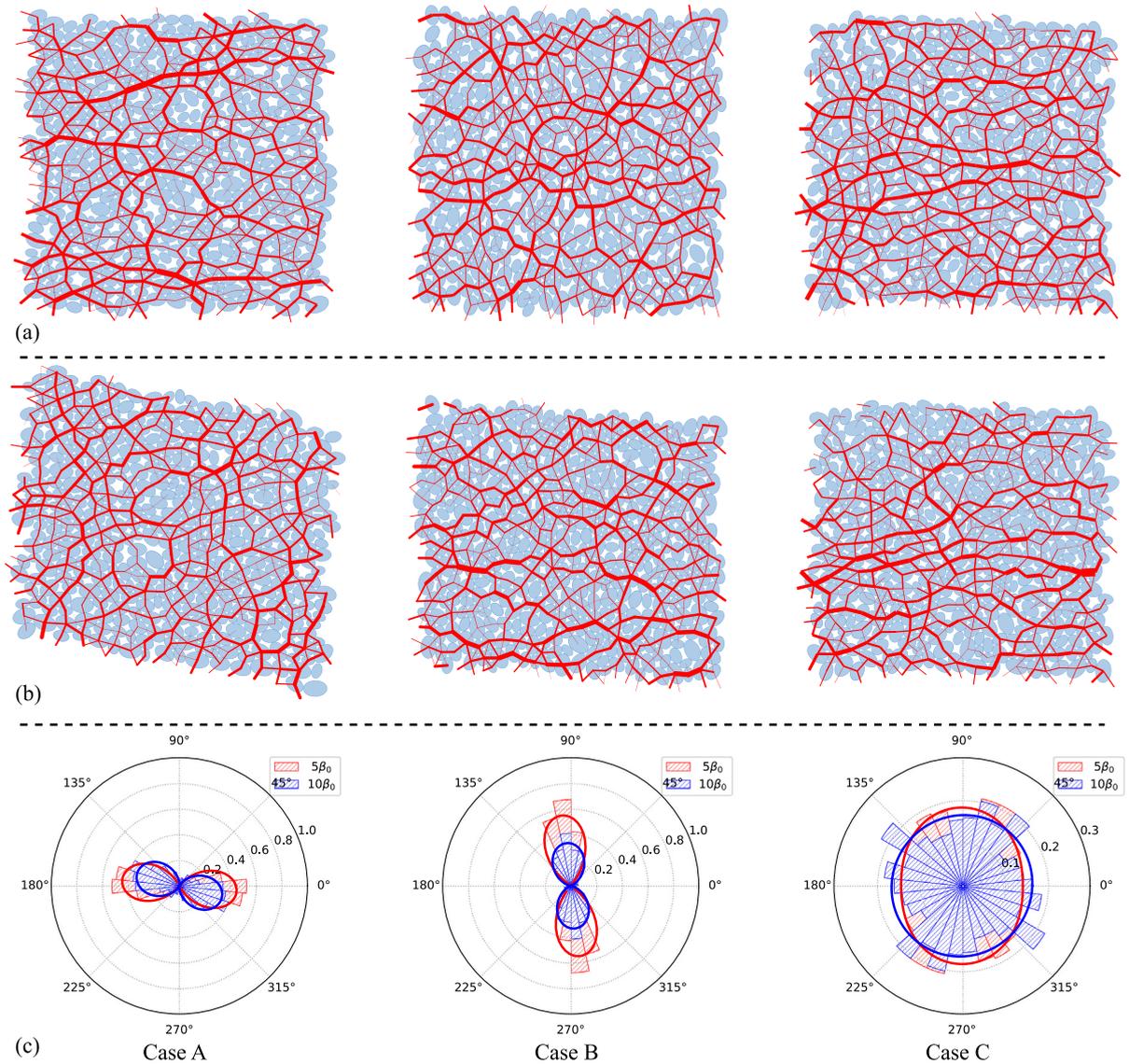
Fig. 21. The force chains of the RVEs of interest in Fig. 20(a-c) with linear thermal expansion coefficient of (a) $5\beta_0$ and (b) $10\beta_0$ and their corresponding distributions of particle orientation for Case A (*left*), Case B (*middle*) and Case C (*right*) after 20 thermal cycles.

which are then solved by two concurrent FEM solvers. At the grain scale, the thermally-induced volume change is seamlessly performed on individual grains, hereby yielding intrinsic coupling of thermo-mechanical response with combining mechanical loading by using DEM. The homogenized response of DEM RVEs composed of finite grains is transferred to the up-scale FEM solvers at Gauss points, and then the up-scale response (temperature change and deformation) is performed back on RVEs. Such a back-and-forth information exchange via RVEs at Gauss points makes the macroscopic thermo-mechanical response physically and smoothly coupled.

Also introduced are two benchmark examples of transient and steady-state thermal conduction with analytical solutions to verify the thermo-mechanical response simulated by the proposed hierarchical coupling approach. Simulated results such as temperature, stress, and deformation are consistent with the analytical solutions. Then, with the proposed approach, we explored the responses of confined granular columns under thermal cycling. It is found that thermal cycling induces granular settlement and stress relaxation, which are positively correlative to thermal perturbation, as reported in the literature, no matter what boundary condition applied. However, the displacement

pattern within a granular column is significantly influenced by both boundary condition and thermal perturbation. We further investigated the effect of inherent anisotropy on the thermo-mechanical response of a granular column composed of elliptic particles. The inherent anisotropy can enhance the resistance of stress relaxation but meanwhile reduce the resistance of granular settlement. The granular column with particles orientating along the thermal cycling direction experiences the most significant granular settlement. Thermal cycling can also make granular materials more isotropic at the microscopic point of view.

Though two-dimensional applications of the proposed approach have been presented in the study. It, however, can be readily extended to three-dimension with the open-source tools *Esys-Escript* [57] and our developed *SudoDEM* [40,47] (https://sudodem.github.io) that formerly support three-dimension. The proposed approach can be further applied to engineering-scale thermal problems, such as analysis of energy piles. Nevertheless, limitations do exist for the proposed approach. Future efforts are required for further improvements such as taking into account the thermal convection of pore fluid for saturated and unsaturated granular materials [71], considering higher fidelity at the grain scale (e.g., thermally-induced particle crushing [72]), and accelerating the simulation with the hybrid CPU/GPU parallelism technique [23,73].

Declaration of competing interest

The authors declare that they have no known competing financial interests or personal relationships that could have appeared to influence the work reported in this paper.

Data availability statement

Source codes and data generated for the study are available.

Acknowledgments

References

[1] M.E. Cates, J.P. Wittmer, J.P. Bouchaud, P. Claudin, Jamming, force chains, and fragile matter, Phys. Rev. Lett. 81 (9) (1998) 1841.

[2] J.N. Roux, G. Combe, Quasistatic rheology and the origins of strain, C. R. Phys. 3 (2) (2002) 131–140.

[3] D.M. Wood, Soil Behaviour and Critical State Soil Mechanics, Cambridge University Press, 1990.

[4] K. Chen, J. Cole, C. Conger, J. Draskovic, M. Lohr, K. Klein, T. Scheidemantel, P. Schiffer, Granular materials: Packing grains by thermal cycling, Nature 442 (7100) (2006) 257.

[5] F. Alonso-Marroquín, H.B. Mühlhaus, H.J. Herrmann, Micromechanical investigation of granular ratcheting using a discrete model of polygonal particles, Particuology 6 (6) (2008) 390–403.

[6] A. Di Donna, L. Laloui, Response of soil subjected to thermal cyclic loading: experimental and constitutive study, Eng. Geol. 190 (2015) 65–76.

[7] S. Zhao, T.M. Evans, X. Zhou, S. Zhou, Discrete element method investigation on thermally-induced shakedown of granular materials, Granul. Matter 19 (1) (2017) 11.

[8] S. Pintaldi, C. Perfumo, S. Sethuvenkatraman, S. White, G. Rosengarten, A review of thermal energy storage technologies and control approaches for solar cooling, Renew. Sustain. Energy Rev. 41 (2015) 975–995.

[9] V. Becattini, T. Motmans, A. Zappone, C. Madonna, A. Haselbacher, A. Steinfeld, Experimental investigation of the thermal and mechanical stability of rocks for high-temperature thermal-energy storage, Appl. Energy 203 (2017) 373–389.

[10] A.K. Sani, R.M. Singh, T. Amis, I. Cavarretta, A review on the performance of geothermal energy pile foundation, its design process and applications, Renew. Sustain. Energy Rev. 106 (2019) 54–78.

[11] S. Na, W. Sun, Computational thermo-hydro-mechanics for multiphase freezing and thawing porous media in the finite deformation range, Comput. Methods Appl. Mech. Engrg. 318 (2017) 667–700.

[12] E. Liu, Y. Lai, H. Wong, J. Feng, An elastoplastic model for saturated freezing soils based on thermo-poromechanics, Int. J. Plast. 107 (2018) 246–285.

[13] J.E. Andrade, Q. Chen, P.H. Le, C.F. Avila, T.M. Evans, On the rheology of dilative granular media: bridging solid-and fluid-like behavior, J. Mech. Phys. Solids 60 (6) (2012) 1122–1136.

[14] N. Guo, J. Zhao, Parallel hierarchical multiscale modelling of hydro-mechanical problems for saturated granular soils, Comput. Methods Appl. Mech. Engrg. 305 (2016) 37–61.

[15] S. Zhao, T.M. Evans, X. Zhou, Shear-induced anisotropy of granular materials with rolling resistance and particle shape effects, Int. J. Solids Struct. 150 (2018) 268–281.

[16] K. Wang, W. Sun, A multiscale multi-permeability poroplasticity model linked by recursive homogenizations and deep learning, Comput. Methods Appl. Mech. Engrg. 334 (2018) 337–380.

[17] P.A. Cundall, O.D. Strack, A discrete numerical model for granular assemblies, Géotechnique 29 (1) (1979) 47–65.

[18] T.S. Yun, T.M. Evans, Three-dimensional random network model for thermal conductivity in particulate materials, Comput. Geotech. 37 (7) (2010) 991–998.

[19] Y. Gan, M. Kamlah, Discrete element modelling of pebble beds: with application to uniaxial compression tests of ceramic breeder pebble beds, J. Mech. Phys. Solids 58 (2) (2010) 129–144.

[20] T. Zhao, Y.T. Feng, An enthalpy based discrete thermal modelling framework for particulate systems with phase change materials, Powder Technol. 354 (2019) 505–516.

[21] M. Baniasadi, M. Baniasadi, B. Peters, Coupled CFD-DEM with heat and mass transfer to investigate the melting of a granular packed bed, Chem. Eng. Sci. 178 (2018) 136–145.

[22] J. Zhao, T. Shan, Coupled CFD–DEM simulation of fluid–particle interaction in geomechanics, Powder Technol. 239 (2013) 248–258.

[23] M. Sousani, A.M. Hobbs, A. Anderson, R. Wood, Accelerated heat transfer simulations using coupled DEM and CFD, Powder Technol. 357 (2019) 367–376.

[24] F. Tu, D. Ling, C. Hu, R. Zhang, DEM–FEM analysis of soil failure process via the separate edge coupling method, Int. J. Numer. Anal. Methods Geomech. 41 (9) (2017) 1157–1181.

[25] A.A. Munjiza, The Combined Finite-Discrete Element Method, John Wiley & Sons, 2004.

[26] A. Munjiza, Z. Lei, V. Divic, B. Peros, Fracture and fragmentation of thin shells using the combined finite–discrete element method, Internat. J. Numer. Methods Engrg. 95 (6) (2013) 478–498.

[27] C. Yan, H. Zheng, A coupled thermo-mechanical model based on the combined finite-discrete element method for simulating thermal cracking of rock, Int. J. Rock Mech. Min. Sci. 91 (2017) 170–178.

[28] G. Ma, Y. Chen, F. Yao, W. Zhou, Q. Wang, Evolution of particle size and shape towards a steady state: Insights from FDEM simulations of crushable granular materials, Comput. Geotech. 112 (2019) 147–158.

[29] H. Meier, P. Steinmann, E. Kuhl, Towards multiscale computation of confined granular media-contact forces, stresses and tangent operators, Tech. Mech. 28 (1) (2008) 32–42.

[30] J.E. Andrade, C. Avila, S. Hall, N. Lenoir, G. Viggiani, Multiscale modeling and characterization of granular matter: from grain kinematics to continuum mechanics, J. Mech. Phys. Solids 59 (2) (2011) 237–250.

[31] Q. Chen, J.E. Andrade, E. Samaniego, AES For multiscale localization modeling in granular media, Comput. Methods Appl. Mech. Engrg. 200 (33–36) (2011) 2473–2482.

[32] N. Guo, J. Zhao, A coupled FEM/DEM approach for hierarchical multiscale modelling of granular media, Internat. J. Numer. Methods Engrg. 99 (11) (2014) 789–818.

[33] V. Kouznetsova, W. Brekelmans, F. Baaijens, An approach to micro-macro modeling of heterogeneous materials, Comput. Mech. 27 (1) (2001) 37–48.

[34] F. Feyel, A multilevel finite element method (FE2) to describe the response of highly non-linear structures using generalized continua, Comput. Methods Appl. Mech. Engrg. 192 (28–30) (2003) 3233–3244.

[35] C.V. Verhoosel, J.J. Remmers, M.A. Gutiérrez, R. De Borst, Computational homogenization for adhesive and cohesive failure in quasi-brittle solids, Internat. J. Numer. Methods Engrg. 83 (8–9) (2010) 1155–1179.

[36] H. Wu, N. Guo, J. Zhao, Multiscale modeling and analysis of compaction bands in high-porosity sandstones, Acta Geotech. 13 (3) (2018) 575–599.

[37] J. Zhao, N. Guo, The interplay between anisotropy and strain localisation in granular soils: a multiscale insight, Géotechnique 65 (8) (2015) 642–656.

[38] G. Mollon, J. Zhao, 3D generation of realistic granular samples based on random fields theory and Fourier shape descriptors, Comput. Methods Appl. Mech. Engrg. 279 (2014) 46–65.

[39] S. Zhao, X. Zhou, Effects of particle asphericity on the macro-and micro-mechanical behaviors of granular assemblies, Granul. Matter 19 (2) (2017) 38.

[40] S. Zhao, J. Zhao, A poly-superellipsoid-based approach on particle morphology for DEM modeling of granular media, Int. J. Numer. Anal. Methods Geomech. 43 (13) (2019) 2147–2169.

[41] Z. Lai, Q. Chen, L. Huang, Fourier series-based discrete element method for computational mechanics of irregular-shaped particles, Comput. Methods Appl. Mech. Engrg. 362 (2020) 112873.

[42] L. Onsager, Reciprocal relations in irreversible processes. I, Phys. Rev. 37 (4) (1931) 405.

[43] Y. Liang, X. Li, A new model for heat transfer through the contact network of randomly packed granular material, Appl. Therm. Eng. 73 (1) (2014) 984–992.

[44] R. Askari, S. Taheri, S. Hejazi, Thermal conductivity of granular porous media: A pore scale modeling approach, AIP Adv. 5 (9) (2015) 097106.

[45] N. Zhang, Z. Wang, Review of soil thermal conductivity and predictive models, Int. J. Therm. Sci. 117 (2017) 172–183.

[46] Itasca Consulting Group, Particle Flow Code (PFC^{3D}), Version 5.0. Minneapolis, MN USA, 2013.

[47] S. Zhao, N. Zhang, X. Zhou, L. Zhang, Particle shape effects on fabric of granular random packing, Powder Technol. 310 (2017) 175–186.

[48] S. Zhao, T.M. Evans, X. Zhou, Effects of curvature-related DEM contact model on the macro-and micro-mechanical behaviours of granular soils, Géotechnique 68 (12) (2018) 1085–1098.

[49] C. Wellmann, C. Lillie, P. Wriggers, A contact detection algorithm for superellipsoids based on the common-normal concept, Eng. Comput. 25 (5) (2008) 432–442.

[50] W.L. Vargas, J.J. McCarthy, Thermal expansion effects and heat conduction in granular materials, Phys. Rev. E 76 (4) (2007) 041301.

[51] J. Christoffersen, M. Mehrabadi, S. Nemat-Nasser, A micromechanical description of granular material behavior, J. Appl. Mech. 48 (2) (1981) 339–344.

[52] J.R. Wren, R.I. Borja, Micromechanics of granular media part II: Overall tangential moduli and localization model for periodic assemblies of circular disks, Comput. Methods Appl. Mech. Engrg. 141 (3–4) (1997) 221–246.

[53] S. Luding, Micro–macro transition for anisotropic, frictional granular packings, Int. J. Solids Struct. 41 (21) (2004) 5821–5836.

[54] J. Desrues, A. Argilaga, D. Caillerie, G. Combe, T.K. Nguyen, V. Richefeu, S. Dal Pont, From discrete to continuum modelling of boundary value problems in geomechanics: An integrated FEM-DEM approach, Int. J. Numer. Anal. Methods Geomech. 43 (5) (2019) 919–955.

[55] J. Choo, Y.J. Kim, J.H. Lee, T.S. Yun, J. Lee, Y.S. Kim, Stress-induced evolution of anisotropic thermal conductivity of dry granular materials, Acta Geotech. 8 (1) (2013) 91–106.

[56] C. O'Sullivan, Particulate Discrete Element Modelling: A Geomechanics Perspective, CRC Press, 2011.

[57] R. Schaa, L. Gross, J. Du Plessis, PDE-based geophysical modelling using finite elements: examples from 3D resistivity and 2D magnetotellurics, J. Geophys. Eng. 13 (2) (2016) S59–S73.

[58] X. Shi, J. Zhao, Practical estimation of compression behavior of clayey/silty sands using equivalent void-ratio concept, J. Geotech. Geoenviron. Eng. 146 (6) (2020) 04020046.

[59] H. Cheng, T. Shuku, K. Thoeni, P. Tempone, S. Luding, V. Magnanimo, An iterative Bayesian filtering framework for fast and automated calibration of DEM models, Comput. Methods Appl. Mech. Engrg. 350 (2019) 268–294.

[60] S. Timoshenko, Strength of Material, Part II: Advanced Theory and Problems, second edition, D. Van Nostrand Company, Inc, New York, 1947.

[61] C. Geuzaine, J.-F. Remacle, Gmsh: A 3-D finite element mesh generator with built-in pre-and post-processing facilities, Internat. J. Numer. Methods Engrg. 79 (11) (2009) 1309–1331.

[62] Y. Zhu, Z. Nie, J. Gong, J. Zou, L. Zhao, L. Li, An analysis of the effects of the size ratio and fines content on the shear behaviors of binary mixtures using DEM, Comput. Geotech. 118 (2020) 103353.

[63] S. Meille, E.J. Garboczi, Linear elastic properties of 2D and 3D models of porous materials made from elongated objects, Modelling Simulation Mater. Sci. Eng. 9 (5) (2001) 371.

[64] N. Guo, J. Zhao, The signature of shear-induced anisotropy in granular media, Comput. Geotech. 47 (2013) 1–15.

[65] S. Falser, S. Uchida, A. Palmer, K. Soga, T. Tan, Increased gas production from hydrates by combining depressurization with heating of the wellbore, Energy Fuels 26 (10) (2012) 6259–6267.

[66] C. Ng, Q. Ma, A. Gunawan, Horizontal stress change of energy piles subjected to thermal cycles in sand, Comput. Geotech. 78 (2016) 54–61.

[67] N. Zhang, T.M. Evans, Three dimensional discrete element method simulations of interface shear, Soils Found. 58 (4) (2018) 941–956.

[68] R. Rusinek, R. Kobyłka, Experimental study and discrete element method modeling of temperature distributions in rapeseed stored in a model bin, J. Stored Products Res. 59 (2014) 254–259.

[69] J. Nie, D. Li, Z. Cao, B. Zhou, A. Zhang, Probabilistic characterization and simulation of realistic particle shape based on sphere harmonic representation and Nataf transformation, Powder Technol. 360 (2020) 209–220.

[70] S. Nadimi, J. Fonseca, Enhancing soil sample preparation by thermal cycling, Géotechnique 66 (11) (2016) 953–958.

[71] P. Rognon, I. Einav, Thermal transients and convective particle motion in dense granular materials, Phys. Rev. Lett. 105 (21) (2010) 218301.

[72] F. Zhu, J. Zhao, A peridynamic investigation on crushing of sand particles, Géotechnique 69 (6) (2018) 526–540.

[73] A. Karatarakis, P. Karakitsios, M. Papadrakakis, GPU accelerated computation of the isogeometric analysis stiffness matrix, Comput. Methods Appl. Mech. Engrg. 269 (2014) 334–355.